Alexandra Müller, BSc

Preparation of a Spongy Nickel-Catalyst with Electron Beam Melting

MASTER'S THESIS

to achieve the university degree of

Diplom-Ingenieurin

Master's degree programme: Advanced Materials Science

submitted to

Graz University of Technology

Supervisor

Assoc.Prof. Dipl.-Ing. Dr.techn. Norbert Enzinger

Institute of Materials Science and Welding

Graz, June 2016

AFFIDAVIT

I declare that I have authored this thesis independently, that I have not used other than the declared sources/resources, and that I have explicitly indicated all material which has been quoted either literally or by content from the sources used. The text document uploaded to TUGRAZonline is identical to the present master‘s thesis.

Date

Signature

Acknowledgment

There are so many people, that I want to thank for their help and support. First of all I would like to thank my main tutor Dipl.-Ing. Dr.techn. Rudolf Vallant for his good advices and the knowledge he shared with me.

Special thanks go to Assoc.Prof. Dipl.-Ing. Dr.techn. Norbert Enzinger for his never ending interest and support concerning every part of my thesis. Despite of his tight schedule he always managed to find time for helping me, whenever I was stuck and in need of input in order to continue with my work. I really appreciate your support!

It was a great pleasure to work with the Institute of Chemical Engineering and Environmental Technology, especially with Dipl.-Ing. Dr.techn. Alexander Schenk, BSc and Assoc.Prof. Dipl.-Ing. Dr.techn. Viktor Hacker. Thank you for the true enthusiasm and the endless support.

In this regard it is very important to mention Ao.Univ.-Prof. Dipl.-Ing. Dr.techn. Reichmann for helping me with the pre-treatment of the starting materials.

Of course I am thankful for everyone at the Institute of Materials Science and Welding for their support throughout this work, but especially I want to thank Leander Herbitschek for providing his practical assistance at the Electron Beam Welding-system. His patience, ease and know-how was one of the main reasons why I enjoyed working at the institute. I also want to thank Gernot Stöfan for his expert knowledge concerning the Scanning Electron Microscopy.

The experiments would not have been so successful without the preliminary tests made by Thomas Spenger. Thank you for your significant help during my thesis.

Most importantly I am thankful for the constant support in the background from my family and friends. I would sincerely like to thank my parents for enabling me to study and their loving care.

This list would not be complete without mentioning the fantastic people I had the pleasure to meet during my study, especially Nina Feldhofer, Michaela Zagler, David Schneider, Georg Weber, Magdalena Truger and Ramona Köppl, who not only were a great moral support, but also provided their knowledge whenever needed.

And more than any other I want to thank Philip, who had to deal with all mood swings and the stress I have been in, but still never got tired of encouraging me all the time. I just cannot thank you enough for your love and support!

Abstract

The objective of the thesis was the formation of a nickel-aluminium alloy with the Electron Beam Welding-system based on the preliminary tests. The desired alloy should consists of the following elements: 48 wt.% Ni, 48 wt.% Al, 2 wt.% Fe and 2 wt.% Cr. This alloy is further leached in potassium hydroxide solution in order to obtain an active skeletal nickel catalyst, which can be used in alkaline fuel cells. Nickel serves as a platinum-free alternative to decrease the production costs of the anode and thus naturally the costs of the fuel cell itself.

Some pretests have already shown, that it is possible to manufacture homogeneous nuggets, consisting of two elements that are completely miscible, in this manner. Very promising results for the melting of copper with nickel gave rise to subsequent experiments with different compositions.

To obtain the targeted Ni-Al alloy, some adaption of the preparation steps were necessary. For this reason new crucibles with higher filling capacities were manufactured. Some of the base materials were grinded to achieve better miscibility of the metal powders.

Initial floating tests were carried out to ensure, that the losses of the fine-grained powder were negligible. Another crucial step was to study the influence of the melting parameters on the quality of the resulting alloys. At the beginning only Ni and Al were alloyed. After optimisation of the melting process, Fe and Cr were added. A spiral beam figure turned out to deliver the best results. Subsequently, series of tests with various frequencies and currents were performed to identify the ideal parameters for manufacturing this alloy.

In the course of all melting experiments it turned out, that the initial state, the test preparation and external factors like temperature and humidity during the prearrangement have a massive impact on the subsequent melting process. In particular, electrostatic charging and oxidation on the surface of Al grains influence the melting behaviour of the materials strongly and in a negative manner.

Scanning Electron Microscopy analysis of the manufactured samples showed major progresses in terms of the homogenisation. Consequently, nuggets were produced using the optimised parameters to measure their catalytic activity afterwards. A few processing steps were necessary to obtain the final catalysts from the nuggets. First, the nuggets had to be pressed and milled, followed by leaching of Al with potassium hydroxide solution to obtain the activated skeletal Ni.

The electrode manufactured with this alloy was then tested in an electrochemical cell. The current-voltage characteristic of the skeletal Ni catalyst was recorded and compared to the results of a commercial catalyst.

Kurzfassung

Das Ziel dieser Diplomarbeit bestand darin, Modellegierungen mit Hilfe der Elektronenstrahlschweißanlage herzustellen. Folgende Zusammensetzung sollte durch diese Methode erreicht werden: 48 Gew.% Al, 48 Gew.% Ni, 2 Gew.% Fe und 2 Gew.% Cr. Diese Legierung kann unter anderem als Katalysator in einer alkalischen Brennstoffzelle als kostengünstige Alternative für Platin eingesetzt werden und erlaubt die Reduktion des Gesamtpreises der Brennstoffzelle. Um eine aktive Legierung zu erhalten, ist es allerdings notwendig, das Aluminium aus der Legierung chemisch herauszulösen, um eine schwammartige Struktur zu erhalten.

Vorversuche zeigten bereits, dass es möglich ist, mittels Elektronenstrahlschmelzen Kupfer und Nickel erfolgreich und homogen miteinander zu verschmelzen. Es muss aber berücksichtigt werden, dass diese beiden Elemente ein vollständig mischbares Legierungssystem bilden, bei der oben genannten Legierung ist das allerdings nicht der Fall.

Es wurden neue Tiegel mit höherem Fassungsvermögen hergestellt, um größere Nuggets zu erhalten. Damit eine gleichmäßige Verteilung der Ausgangsmaterialien im Tiegel erreicht werden konnte, wurden sie zuerst in einer Kugelmühle gemahlen, um kleinere Korngrößen zu erhalten.

Zu Beginn wurden Flutungsversuche durchgeführt, um sicherzustellen, dass die Verluste der Materialien beim Spülen der Kammer vernachlässigbar sind. Anschließend wurde der Einfluss der Schweißparameter auf den Aufschmelzvorgang untersucht. Die Versuche wurden anfangs nur mit Al und Ni durchgeführt. Sobald die idealen Parameter gefunden wurden, konnten die gewünschten Mengen an Fe und Cr hinzugefügt werden.

Im Laufe der Aufschmelzversuche stellte sich heraus, dass eine spiralförmige Strahlfigur die besten Ergebnisse lieferte. Außerdem wurde festgestellt, dass der Ausgangszustand der Materialien und vor allem äußere Einflüsse, wie Temperatur und Luftfeuchtigkeit während der Probenvorbereitung, sich entscheidend auf den Schweißvorgang auswirken. Insbesondere elektrostatische Aufladungen und Oxidation an der Oberfläche der Aluminium-Körner wirken sich äußerst negativ auf das Aufschmelzverhalten aus.

Die hergestellten Proben wurden anschließend mittels Rasterelektronenmikroskopie untersucht und zeigten, dass diese deutlich homogener waren, als die Nuggets der Vorversuche. Mit Hilfe der Erkenntnisse aus der Parameterstudie wurden neue Proben hergestellt, um die katalytische Aktivität der Legierung in Brennstoffzellen zu messen.

Davor waren allerdings noch einige Bearbeitungsschritte notwendig, um die erhaltenen Nuggets zu zerkleinern. Zuerst wurden sie gepresst und in einer Kugelmühle gemahlen. Das Aluminium wurde anschließend mit einer Kalilauge herausgelöst, um das Nickel zu aktivieren. Das so entstandene Pulver wurde zu einer Elektrode weiterverarbeitet und in einer elektrochemischen Zelle getestet. Dazu wurde eine Strom-Spannungs-Kennlinie aufgenommen und mit der eines kommerziell erhältlichen Raney®-Nickel verglichen.

Contents

1 Introduction

The effects of global warming are increasing every year and therefore leading to serious problems, which cannot by denied anymore. According to statistics released in 2014, an average amount of 8.513 kWh/year is consumed per capita in Austria[1], in the United States even 12.985 kWh/year.

The main part of the required energy is produced by combustion of fossil fuels leading to severe air pollution. Carbon dioxide, one of the primary greenhouse gases, gathers in the atmosphere, absorbing the solar radiation reflected on the earth's surface. Normally, the sunlight is released into space again after reflection on the surface of the earth, but greenhouse gases absorb the heat and the atmosphere's temperature increases. The increase of the average global temperature leads to melting of ice, rising of the sea level and to severe weather conditions in general. The main sources of greenhouse emission in the United States are as follows: 30% electricity, 26% transportation, 21% industry, 12% commercial and residental and 9% agriculture. According to this data, transportation is the second biggest source of greenhouse gas emission[2]. Thus, different kinds of alternative fuels like solar power, electricity, natural gas and many more need to be promoted, in order to decrease human's influence on the environment.

One highly promising technology are fuel cells. There, a chemical reaction between hydrogen and oxygen produces electrical energy, heat and water. In comparison to conventional combustion of hydrocarbons, no carbon-dioxide is emitted, only water. Nevertheless, fuel cells are hardly used yet, because there are still some challenges to overcome. One reason is the necessity of a catalyst. Currently, the catalyst mainly consists of platinum supported on carbon. Platinum is a very rare metal, hence only available at high price. Needless to say, this increases the price of the catalyst and logically the one for the whole fuel cell.

By providing a platinum-free catalyst for Alkaline Fuel Cells (AFC), this alternative technology will be more competitive in the future. One of the most promising alloys for this application is a spongy nickel-catalyst. It is usually doped with small amounts of metals like Fe, Cr, Ti and Mo to elevate the catalytic activity and stabilise the alloy.

To promote the economic competitiveness of the AFC, one attempt is to find another way to produce target compositions by fast alloying of precursor metal powders. This can be done by melting powdery base materials in an Electron Beam Welding-system, to achieve an alloy with defined properties.

2 Basics

2.1 Electron Beam Welding

Electron Beam Welding (EBW) is a melting technique, where highly accelerated and focused electrons are directed onto the surface of a workpiece using magnetic fields. When the electrons hit the sample, they get decelerated and the kinetic energy is converted into thermal energy. The material starts to melt and the weld is formed after cooling.

One of the most important parts of the EBW is the beam source. It should generate a beam as narrow as possible with variable power. Inside the beam source, cathodic material (e.g. a tungsten wire) is heated electrically to enable emission of electrons. By applying a voltage usually in the range of 60-150 kV the electrons are accelerated towards an annular anode. Through the hole in the anode, the electrons can be directed towards the workpiece[3].

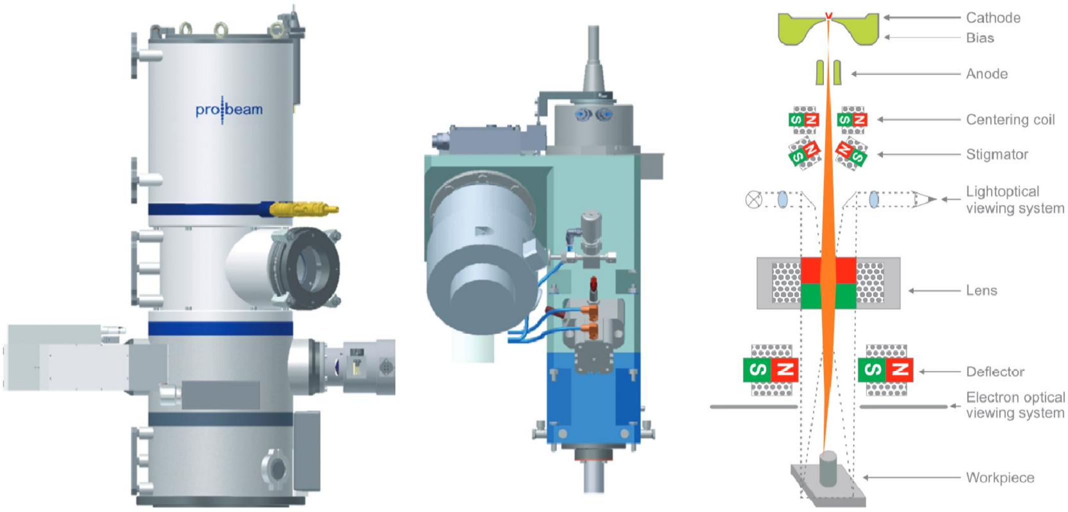

Figure 2.1: Schematic representation of the EBW: High-voltage column (left), low-voltage column (centre) and electron beam column (right)[3].

The centering coils are located right after the annular anode. These coils (see Figure 2.1) act as magnetic lenses and focus the electron beam onto the sample. Due to the magnetic fields in the coil, the beam can be deflected very fast. With a stigmator, an occurring astigmatism of the beam is compensated. The lenses are located below the stigmator and enable the modification of the beam diameter. A system of four coils, called deflector, produces a magnetic field and positions the electron beam.

When the electrons hit the workpiece, the material starts to melt and also partly evaporates forming the weld pool. The penetration depth of the electrons into the surface is usually below 0.1 mm, depending on the beam energy and the material's density.

Despite of the low penetration depth, the welding depths can be several centimeters. The high-energy electrons melt and even vaporise the material under formation of a capillary. This so-called keyhole facilitates further penetration of the beam into the target material[4]. The whole process has to be operated under high vacuum ($< 10^{-4}$ Pa), to prevent scattering of electrons on air molecules.

Using EBW to form welds provides many advantages, starting with a good reliability and efficiency, as well as a very high power density (up to 10^7 W.cm^{-2}). Nearly all materials, that are electrically conductive, can be welded in this manner and a wide range of material thicknesses can be fused. Thus many different applications are possible. Due to the fact, that the whole melting process is performed under high vacuum, no shielding gas is required. One of the many advantages concerning the following experiments is the weldability of dissimilar materials, due to the high energy density of the electron beam. Thus, even metals with particularly diverse melting points and thermal conductivities can be welded successfully using this method [5,6].

2.1.1 Electron Beam Melting

Electron Beam Melting (EBM) is one of the most important methods for additive manufacturing of metal parts. In this process, the raw material (e.g. metal powder) placed on the sample stage, is partly melted layer by layer using a directional electron beam focused on the surface.

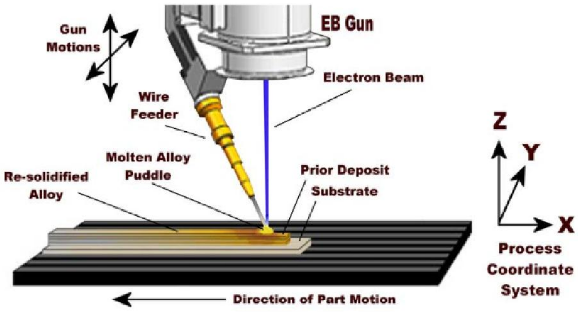

Figure 2.2: EBM principle: The electron gun generates an electron beam directed onto the substrate. In this case the material is added to the molten alloy puddle by a wire feeder. Step by step one layer is melted onto the prior deposit [4].

The schematic principle is shown in Figure 2.2. After one layer is finished, the stage moves downwards, the powder is added and again melted locally. Each layer is build up according the given 3D-model. Repeating this process over and over again, the desired part can be produced step by step. These melting processes have to be performed under high vacuum, in order to prevent the electron beam from deflections, as discussed above.

The quality of components produced with EBM depends on the process parameters, as well as the material and its properties. Especially, when melting powders or liquids, the energy source and the material composition have huge influence on the resulting component. However, the beam parameters determine the penetration depth and the weld pool geometry and consequently, the melting and solidification processes. Among others, the following main beam parameters can usually be regulated: beam current, acceleration voltage, focus point, spot velocity and beam pattern[7].

If the process parameters are not adjusted accurately, negative effects such as the splattering of powder particles can occur, due to electrostatic charging of material grains. A high electrical resistance is build-up at the contact points of the particles, hindering the discharge of the charge carrier. Subsequently, an electrostatic charge remains, initiating repulsion between two equally charged particles. Assuming the powder particles are globular, the electrical charge Q_g is calculated using the following equation[7]:

$$Q_g = \eta I t$$

$$\begin{aligned} Q_g ... Charge\ [C], \\ I ... Current\ [A], \\ t ... Time\ [s], \\ \eta ... Part\ of\ electrons\ remaining\ on\ the\ grain\ (ca.\ 1\%) \end{aligned} \tag{2.1}$$

Using Coulomb's law the repulsive force of two equal sized and charged grains can be determined:

$$F_{rep} = \frac{1}{4\pi\epsilon_0} \cdot \frac{Q_g^2}{d_g^2}$$

$$\begin{aligned} F_{rep} ... Repulsive\ force\ [N], \\ Q_g ... Charge\ [C], \\ d_g ... Distance\ between\ the\ charges\ [m], \\ \epsilon_0 = 8.854\ .\ 10^{-12} ... Electric\ constant\ [F.m^{-1}] \end{aligned} \tag{2.2}$$

Apart from electrostatic charging, mechanical, electrodynamic and thermodynamic effects contribute to the splattering of particles. However, these effects are usually insignificant.

Thermodynamics of the Melting Process

Heating a solid material to a certain temperature requires a specific energy, depending on the material's properties. This can be estimated using the following formula:

$$E_m = m\left[\int_{T_0}^{T_m} c_{p,l}(T)dT + H_M + \int_{T_m}^{T} c_{p,s}(T)dT\right]$$

$$\begin{aligned} E_m...Energy\ demand\ [J] \\ m...Mass\ [kg] \\ T_0...Starting\ temperature\ [K] \\ T_m...Melting\ temperature\ [K] \\ H_m...Heat\ of\ fusion\ [J/kg] \\ c_{p,l}, c_{p,s}..Heat\ capacity\ of\ liquid\ and\ solid\ state\ [J/kg.K] \end{aligned} \tag{2.3}$$

According to Equation 2.3, the energy demand depends on the properties of the liquid, as well as of the solid state of the material. For the following experiments this formula was used, to calculate the required energy demand for melting different base materials. The value E_m obtained from Equation 2.3, is further needed to estimate the beam parameters, using the following Equation 2.4:

$$P_b = U_b \cdot I_b = \frac{E_m}{t_b}$$

$$\begin{aligned} P_b...Beam\ power\ [W] \\ U_b...Acceleration\ voltage\ [kV] \\ I_b...Beam\ current\ [mA] \\ E_m...Energy\ demand\ [J] \\ t_b...Impact\ time\ [s] \end{aligned} \tag{2.4}$$

2.2 Fuel Cell

Fuel cells (FCs) convert chemical energy directly into electrical energy. Therefore, the efficiency is a lot higher, than in conventional combustion engines. FCs basically consist of two electrodes and an ion conducting electrolyte in between. The electrodes are coated with a catalyst, usually platinum. Additionally, anode and cathode need to be porous with a high surface area, in order to ensure a maximum contact between electrodes and electrolyte[8]. A constant supply of a fuel e.g. hydrogen (H_2) and oxygen (O_2) is necessary to enable ongoing reactions. Energy is produced by reactions between oxygen and hydrogen. H_2 is oxidised at the anode producing H^+ and electrons. The electrons migrate through an external circuit and generate an electric current. Subsequently, the H^+ ions migrate to the cathode through the electrolyte. At the cathode, oxygen is supplied and catalytically reduced. Thereby, electrons are absorbed and O^{2-} is formed.

Fuel Cells offer a lot more advantages apart from high efficiency, like low emission, high durability, low noise and very good power density[9].

2.2.1 Alkaline Fuel Cell

The Alkaline Fuel Cell (AFC) was very popular in the 1970s and 1980s, due to its application in aerospace. Subsequently, great improvements with another type of FC, called Proton Exchange Membrane Fuel Cell (PEMFC), were achieved. Therefore, the interest in AFC decreased. With new ideas to lower the costs, AFCs might be applicable for terrestrial use as well. By replacing platinum in the anode with non-noble metals, notable progresses are observable and give rise to renewed interest in this FC type. Examples for promising materials for the anode are nickel boride, sintered nickel and Raney®-Ni, amongst other[10].

The mobile ion in an AFC is OH^- and the typical operation temperature is in the range of 50-200 °C. It was used in space vehicles (e.g. Apollo), the only application worth mentioning so far[8].

Principle of Operation

In AFCs hydroxyl ions are generated at the cathode and move towards the anode, where OH^- reacts with H_2 to water and produces electrical energy. Usually potassium hydroxide (KOH) solution is used as electrolyte, due to low cost and good properties. The following chemical reactions take place in AFCs[11]:

$$\begin{aligned} Anode\ reaction: &\quad 2H_2 + 4OH^- \rightarrow 4H_2O + 4e^- \\ Cathode\ reaction: &\quad O_2 + 2H_2O + 4e^- \rightarrow 4OH^- \\ Cell\ reaction: &\quad 2H_2 + O_2 \rightarrow 2H_2O \end{aligned} \tag{2.5}$$

Apart from electrical energy, heat and water are generated and have to be removed constantly, to enable a continuous reaction. The electrode is usually a compound material consisting of two layers, an active catalyst layer on top of a hydrophobic gas diffusion layer. Typically, the compound is pressed onto a conducting metal. It has to be mentioned, that the assembly of electrodes has a great impact on the AFC's performance.

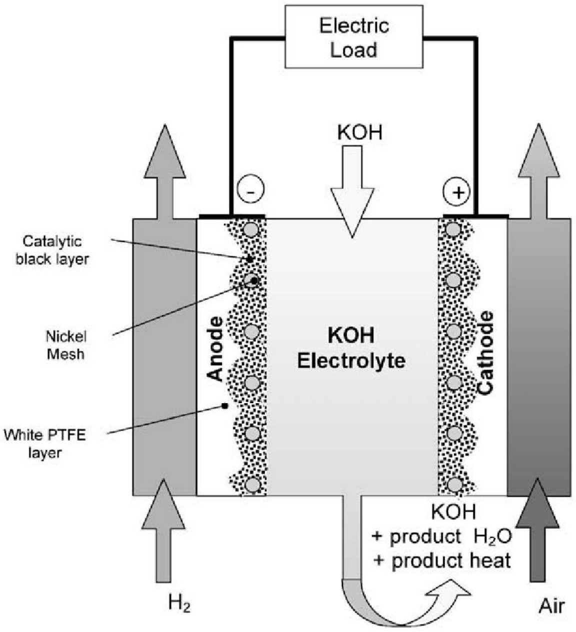

Figure 2.3: Schematic principle of the AFC[12].

Catalyst

Catalysts accelerate chemical reactions, elevate the selectivity and therefore prevent the production of unwanted side-products. For hydrogenation nickel is often used as catalyst. The performance of a catalyst is improved by increasing the surface area. Thus, the nickel should be fine-granular. One way to achieve this, is the preparation of a spongy nickel by leaching out aluminium of an nickel-aluminium alloy[13].

The properties of the catalyst, such as activity and selectivity can be enhanced by adding small quantities of other elements to the catalyst material. These so called promoters are usually added to the melt. Common examples are chromium, iron, copper, molybdenum, cobalt and titanium.

2.3 Investigation Techniques

2.3.1 Scanning Electron Microscopy

In a Scanning Electron Microscope (SEM) a focused electron beam is scanned across the sample's surface to obtain information about topography, crystal orientation and material composition. The schematic diagram of a SEM is shown in Figure 2.4. Electrons are emitted by an electron gun (cathode), either by a thermionic emission, field emission or both. The electrons are then accelerated towards the anode and focused by the Wehnelt cylinder. Condenser lenses define the convergence angle and the size of the illuminated spot and forming a narrow beam. With pairs of scanning coils, the beam is deflected and focused. The energy of the electron beam can usually be varied within the range of 0.2 keV to 40 keV. Additionally, the whole process has to be carried out under high vacuum, to prevent scattering of the beam by particles in gas atmosphere[14].

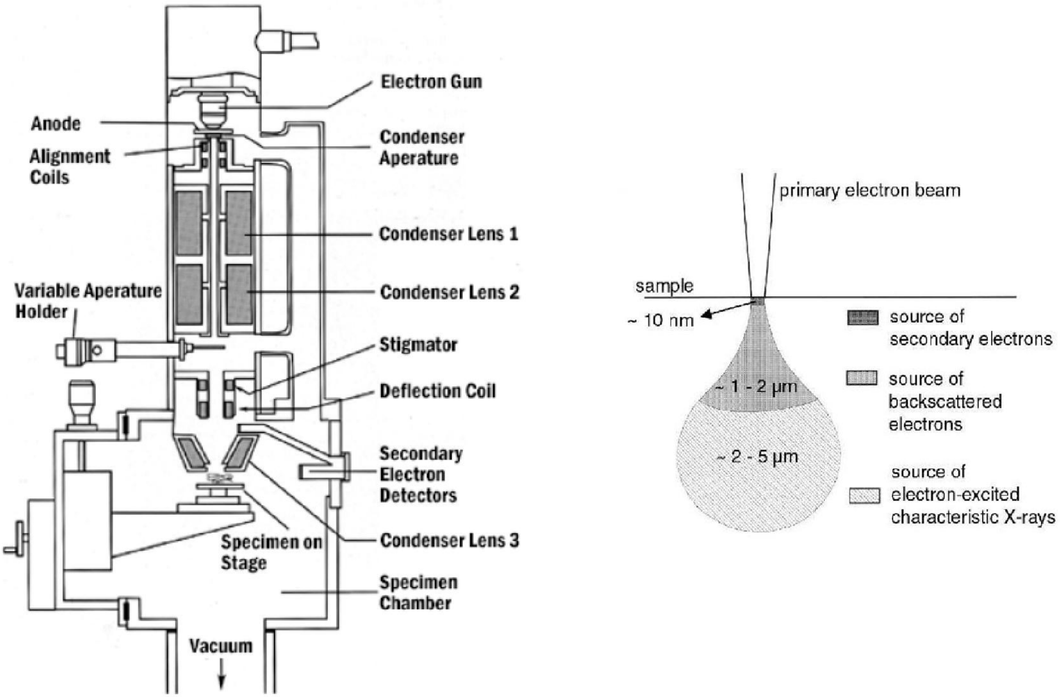

Figure 2.4: (a) Schematic diagram of the SEM principle (b) interaction volume of Secondary Electrons (SE), Backscattered Electrons (BSE) and X-rays[15,16].

When primary electrons hit the sample, secondary electrons are emitted and collected by an electron detector. After amplification and quantification the local distribution is then displayed on the screen.

Two different types of electrons are generated and provide various details about the investigated material[17]:

Secondary Electrons (SE): SE are generated by inelastic scattering of the primary beam at the surface of the sample (Figure 2.4). Due to their very low energy, they origin from the top few nanometers and thus reflect the topography. The SE-yield depends on the surface's slope and further on the detector's position. Protruding parts of the sample generate more SE, thus appear brighter. Whereas cavities seem darker. The SE-signal is detected by a scintillator-photomultiplier-system called Everhart-Thornley-detector. When the electrons hit the scintillator, light is generated and transmitted to the photomultiplier, that converts photons into electron pulses.

Backscattered Electrons (BSE): The BSE signal results from elastic scattering. The primary electrons penetrate the sample, are scattered multiple times at a large angle, leave the surface again and are detected. The number of BSE depends on the atomic number (Z) at a very high degree and therefore the resulting signal contains information about the material contrast. Areas with a high average Z appear brighter in the image due to the low penetration depth. The detection is usually operated by a solid-state detector. Depending on the energy, the incoming electrons generate a certain amount of electron-hole pairs, that can be further processed as a signal.

Energy Dispersive X-ray Spectroscopy (EDX)

EDX is a very powerful tool for chemical analysis, where the interaction of the electron beam and the sample generates a characteristic X-ray signal.

The principle of this technique is shown in Figure 2.5. When an inner shell electron gets kicked out by an incoming electron of the beam, a hole is left in this shell. Another electron from a higher shell refills this vacancy by releasing the excessive energy in the form of a characteristic X-ray. This released energy is equal to the energy gap between the involved shells. These X-ray signals are detected, providing information of the quantitative chemical composition of an unknown sample[18].

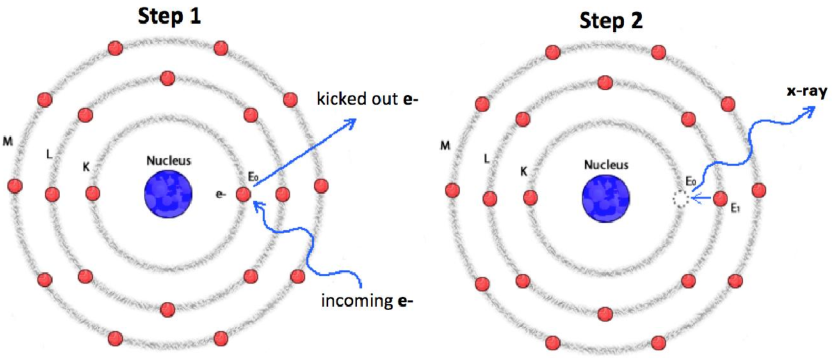

Figure 2.5: Principle of EDX. Step 1: Inner shell electron (K-shell) is kicked out by an incoming electron. Step 2: An electron from L-shell refills the vacancy in shell K under emission of X-rays with characteristic energy[19].

Elemental Mapping

Another additional method, called elemental mapping enables the determination of the elemental distribution on the surface of an investigated sample. The single elemental maps are combined and overlapped to obtain the elemental distribution. With this technique, it is possible to identify inclusions, phases with different compositions and impurities. For the following experiments it was applied, to detect non-melted base material.

2.3.2 Microhardness Tests

Hardness is defined as resistivity of a material against the penetration of a harder matter. It can be calculated by the ratio of the compressive force F to the area of indentation A. Hardness measurements are often used as quality check or to identify the state of the material[20].

$$H = \frac{F}{A}$$

$$\begin{aligned} H...Hardness \\ F...Compressive\ force\ [N] \\ A...Area\ of\ indention\ [mm^2] \end{aligned} \tag{2.6}$$

If the hardness of small areas of a material or just a single crystallite is measured, it is referred to as microhardness. Three common test methods can be applied to investigate metals: Brinell, Rockwell and Vickers. In this thesis, Vickers hardness test was performed, thus only this method is described in detail.

Vickers hardness HV: The principle of the microhardness measurement is shown in Figure 2.6. A quadrangular diamond pyramid with an opening angle of 136° is used as an indenter. With a test load F it is pressed against the surface of a sample for 10 s to 15 s. From the dimensions of the test indentation the microhardness is evaluated.

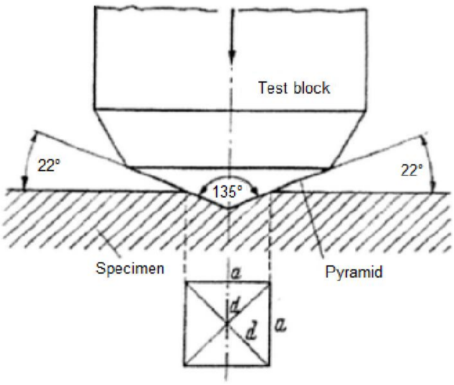

Figure 2.6: Schematic principle of the Vickers hardness test [20].

Using the following equation, the Vickers hardness can be calculated:

$$HV = 0,189 \cdot \frac{F}{d^2}$$

$$\begin{aligned} HV...Vickers\ hardness \\ F...Test\ load\ [N] \\ d...Arithmetic\ mean\ of\ the\ two\ diagonals\ [mm] \end{aligned} \tag{2.7}$$

In order to obtain valid results, the distance between two indentation has to be at least 5d. In addition, a minimum thickness of 100 μm is required, when testing soft layers. For hard layers, a thickness of 80 μm is sufficient. When the requirements mentioned above are fulfilled, Vickers hardness measurements can be applied for a wide range of materials.

2.4 Materials

As mentioned above, four different materials were used for the following experiments. To compare the properties of these materials, some basic information is listed in Table 2.1.

Table 2.1: Overview of the material properties: Atomic number Z, molar mass M, density ρ, melting point T_m, boiling point T_b, fusion heat ΔH_{fus}, thermal conductivity λ, thermal expansion/linear expansion coefficient α_l, energy demand for melting E_m and magnetism[21,22,23]

	Ni	**Al**	**Fe**	**Cr**
Z	28	13	26	24
M [g.mol^{-1}]	58.71	26.98	55.85	51.996
ρ [g.cm^{-3}]	8.9	2.7	7.9	7.19
T_m [°C]	1453	660	1536	1890
T_b [°C]	2732	2467	2750	2672
ΔH_{fus} [J.g^{-1}]	301	398	268	314
λ [W(m.K)$^{-1}$]	85	200	80	94
α_l [10^{-6}.K^{-1} at 20°C]	13.0	23.0	12.2	6.2
Magnetism	ferromag.	paramag.	ferromag.	antiferromag.

2.4.1 Nickel

Nickel has a density of 8.9 g.cm^{-3} and its hardness is moderate. It is forgeable and ductile. Due to the face-centered cubic structure (fcc) of pure nickel, it shows good working properties. Furthermore, it is ferromagnetic up to the Curie-temperature of 360 °C[14].

One of the main advantages of nickel is the high corrosion-resistance, which makes it economically interesting. Therefore, it is used in stainless steels and in nickel-based alloys. Additionally, Ni shows high resistance to air, water and bases at room temperature. By adding just small amounts of alloying elements, the high temperature strength and resistance can be increased[24,25].

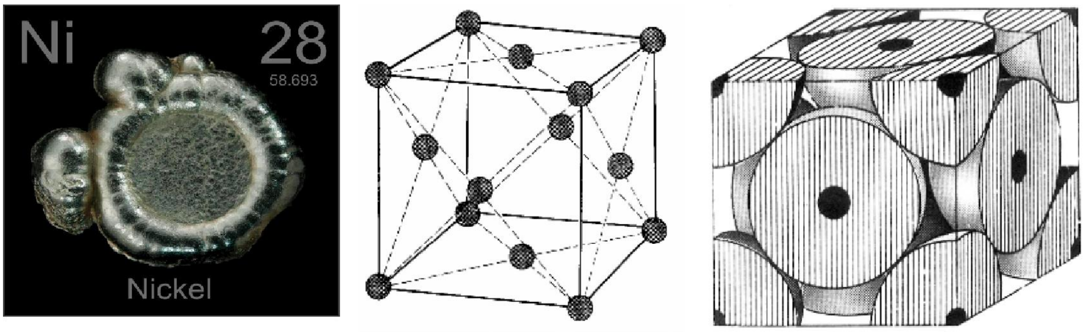

Figure 2.7: Nickel button and the fcc-crystal structure[25,26].

Concerning the thermal properties, vapour pressure and thermal expansion had to be taken into consideration for the experiments. The coefficient of thermal expansion of pure nickel (99.94%) can be seen in the following Figure 2.8. A prominent peak is visible at the Curie point. The thermal expansion can be influenced by chemical composition, microstructure and degree of deformation[24]. In addition, the vapour pressure curve is displayed as well.

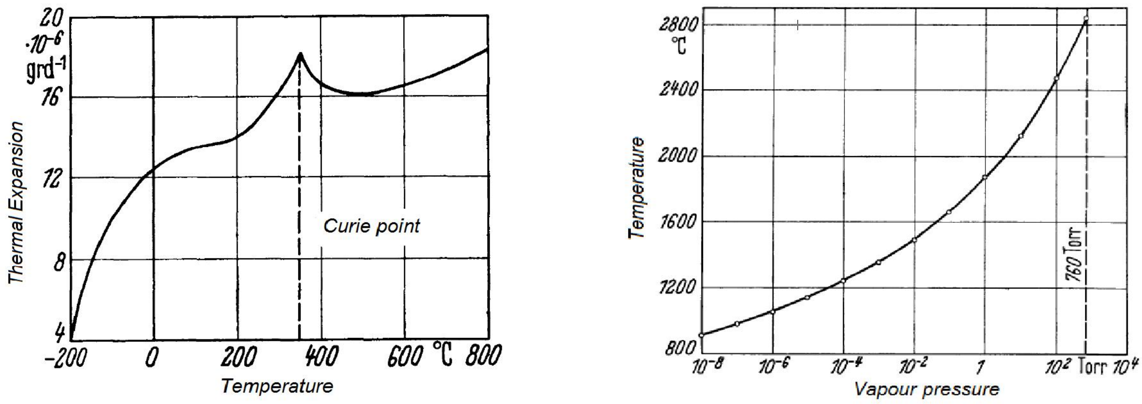

Figure 2.8: Temperature dependency of thermal expansion of Ni (left) and vapour pressure curve (right)[24].

Dangers: Nickel and its alloys are highly allergenic and moreover have a carcinogenic potential. Another danger lies in inhaling of dust and skin contact. Nickel is one of the metals, that most frequently triggers contact allergies.

2.4.2 Aluminium

Aluminium is the most commonly used metallic material, especially when high strength and low weight are required. It is three times lighter than steel, corrosion-resistant due to the oxide-layer and shows a high stability. Furthermore, the heat- and electric conductivity is good, but the high thermal expansion could cause problems when processing. The melting point (T_m = 660 °C) is quite low compared to the other materials, that are used during the following experiments. The crystal structure is fcc and no lattice transformations take place[14].

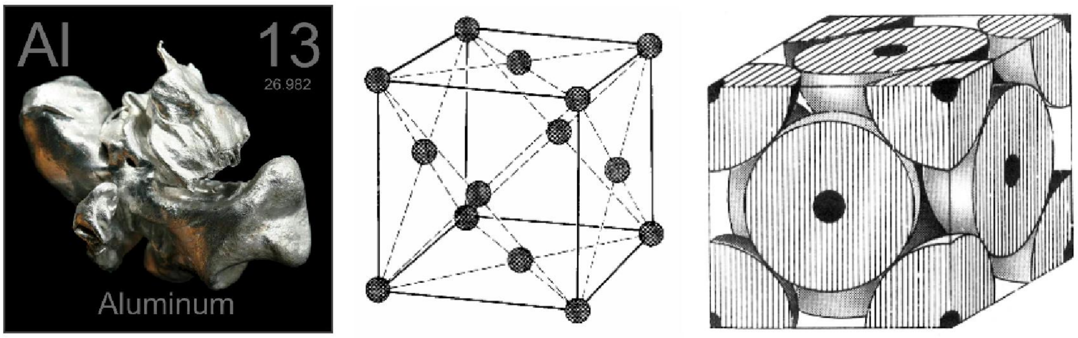

Figure 2.9: Aluminium nodule produced by pouring melt (left) and the fcc-crystal structure (right)[25,26].

Under ordinary conditions a protective layer of aluminium oxide builds up on the surface of aluminium within seconds. Thus, it does not react with water instantly.

Dangers: One of the great dangers of aluminium powder is the high flammability. When it gets into contact with water, highly flammable hydrogen can be generated, causing an additional risk of explosion. Furthermore, the intense electric charging can induce discharging, which can then spark the aluminium dust cloud[27].

Aluminium-Oxide

An oxide layer is easily formed when Al is exposed to air at room temperature. Compared to steel, there is only one oxide observable (Al_2O_3). It melts at very high temperatures (T_m = 2072 °C)[28].

$$4Al + 3O_2 \rightarrow 2Al_2O_3 \quad \Delta H = -1676\ kJ/mol \tag{2.8}$$

One advantage of the oxide film is the enhanced corrosion resistance. However, at the same time the electrical non-conducting layer lowers the weldability and therefore, has to be removed previously. For a granular material this cannot be performed easily, thus preventing a too high degree of oxidation is required in the first place by protecting the Al from excessive exposure to air. It should also be taken into consideration, that as soon as the oxide layer is removed, a new one starts to form instantly, due to the high reactivity of Al with O_2.

2.4.3 Iron

Iron is ferromagnetic with a white-silver coloured surface. It can be easily processed due to its high ductility and tensile strength. When exposed to air, it reacts with oxygen under formation of different oxides and hydroxides. The thermal, as well as the electrical conductivity is very high. Fe is one of the metals with allotropical properties, thus it exists in two different crystal structures in the same physical state. The crystal structure of pure Fe at room temperature (also known as α-iron) is body-centered cubic (bcc) and is shown in Figure 2.10. When heated up to 912 °C, the crystal structure of Fe changes from bcc to fcc and at 1394 °C back to bcc again[14]. Pure iron is hardly ever used, but significant as an alloy. Technically speaking one of the most important applications is the manufacturing of steel, where the properties are heavily influenced by adding carbon[23].

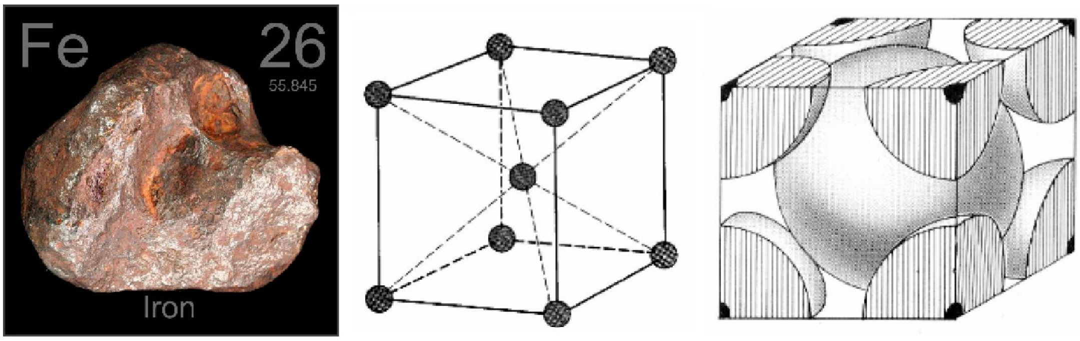

Figure 2.10: Meteorite mostly consisting of iron and its bcc-crystal structure[25,26].

Dangers: Inhaling excessive concentrations of iron oxide vapour or dust is one of the dangers and can even increase the risk of lung cancer. Another risk lies in high ignitability and flammability[21].

2.4.4 Chromium

Chromium is a silver-gray, highly corrosion resistant, hard and brittle metal. At its primitive state it is form- and forgeable. Cr is mainly used for chromium-plating as protection against corrosion or wearing and also for decorative reasons. Furthermore, it appears in some non-ferrous alloys and heat-resistant, non-corroding steels[14]. The protective layer is formed instantly when reacting with oxygen, leaving a thin, hard oxide film that prevents the metal from further corrosion. Concerning thermal properties, Cr shows a high heat conduction, that decreases with increasing temperature. Additionally, it shows a high thermal expansion. At a temperature of 37 °C, Cr changes from antiferromagnetic to paramagnetic. Subsequently, the thermal expansion increases massively.

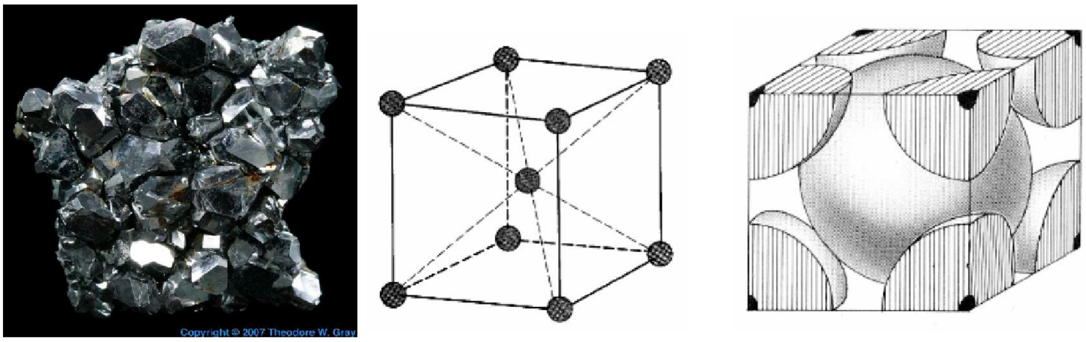

Figure 2.11: Electrodeposited chromium crystal and the bcc-crystal structure[25,26].

Dangers: Chromium in small amounts is harmless, however when it exceeds a certain amount it can cause allergic reactions, like rashes and sore throat. In the worst case, further effects on health can be damages of kidney and liver, weakening of the immune system and change in the genetic material[21].

2.4.5 Ni-Al

When Ni and Al are melted, a Ni-Al binary system is formed. To predict the phases, that appear at certain compositions, the phase diagram shown in Figure 2.12 is required. With a composition of 50 wt.% Ni and 50 wt.% Al, phases Ni_2Al_3, $NiAl_3$ and $NiAl_3$-Al-eutectic are observeable.

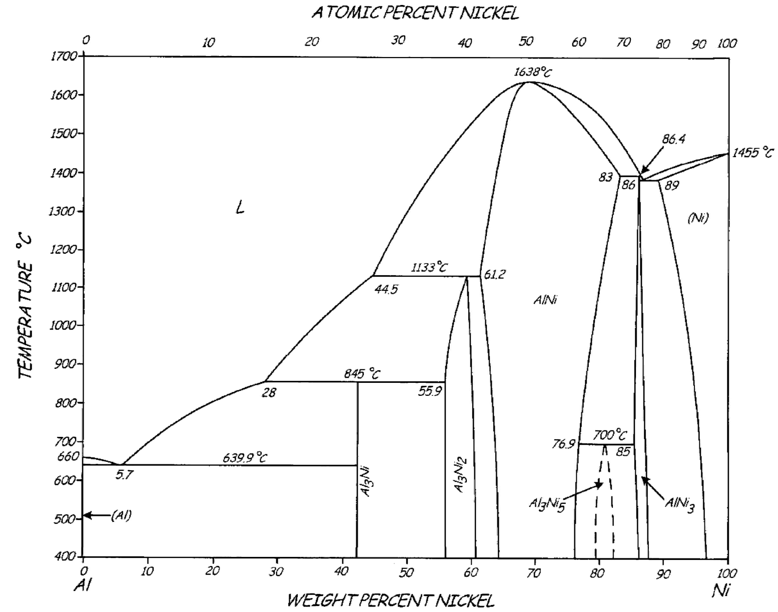

Phase	Composition wt.% Ni
(Al)	0 to 0.24
Al_2Ni	42
Al_3Ni_2	55.9 to 60.7
AlNi	61 to 83.0
Al_3Ni_3	79 to 82
$AlNi_3$	85 to 87
(Ni)	89.0 to 100

Figure 2.12: Ni-Al phase diagram[29]

Former investigations showed, that small quantities of added **chromium** dissolve into Ni_2Al_3- and $NiAl_3$-phases. If the alloy is quenched quickly, chromium gathers between the dendrites and form a supersaturated solid solution. The presence of chromium lowers the reactivity of the alloy with bases, thus it takes longer to leach the aluminium out. It is assumed, that chromium hinders the leaching process and stabilises the alloy. At around 2 wt.% Cr this effect is maximal.

When **iron** is added to the Ni-Al alloy, it substitutes nickel in Ni_2Al_3-phase up to 10 wt.%. Due to the presence of Fe, the surface area is increased and thus the activity too. At around 6 wt.% Fe the activity reaches its maximum[13].

2.4.6 Spongy Nickel

Spongy Ni can be used as a highly active catalyst on the anode side of alkaline H_2/O_2 - fuel cell. Not only can it catalyse the H_2-oxidation, it is also capable of absorbing and reversibly storing huge amounts of hydrogen. Hence, spongy Ni electrodes are not affected by short excess of H_2 or interruption of the H_2-supply[30].

The skeletal Ni structure is produced by leaching a Ni-Al alloy in alkaline solution to obtain a porous structure. The remaining spongy Ni can then be used as a catalyst for hydrogenation, mainly of unsaturated organic compounds. To sustain an optimised leaching behaviour, the Al fraction should be in between the range of 50-70 wt.%. [13]

In the course of the leaching process with a sodium hydroxide solution (NaOH), the following reaction of the Ni-Al alloy takes place:

$$Al + NaOH + 3H_2O \rightleftharpoons NaAl(OH)_4 + 3/2H_2 \tag{2.9}$$

At the beginning Al is leached out of the eutectic, followed by the removal of Al from the intermetallic phases. It can be assumed, that the phases undergo these transformation steps:

$$NiAl_3 \rightarrow Ni_2Al_3 \rightarrow NiAl \rightarrow Ni_3Al \rightarrow Ni \tag{2.10}$$

According to these steps, the attack starts at the phase with the highest Al concentration. However, the $NiAl_3$-Al-alloy is transformed directly into Ni[31].

After leaching, the Ni sponge needs to be stored under water or ethanol, to prevent reactions of nickel with air to nickel oxide:

$$2Ni + O_2 \rightarrow 2NiO \tag{2.11}$$

During the leaching process (Equation 2.9), hydrogen is already stored in the sponge, partly adsorbed at the surface and also dissolved in the nickel lattice. The reversible stored hydrogen is responsible for the catalytic activity. It is assumed, that the remaining Al stabilises the Ni sponge. It has to be mentioned, that skeletal Ni is highly pyrophoric. Thus, it has to be handled under inert atmosphere.

When spongy Ni is heated, Ni particles start to sinter and the lattice defects anneal. Furthermore, hydrogen desorbs and the catalyst's activity drops to zero.

Manufacturing of a spongy Nickel

Currently there are three different methods to produce spongy Ni:

- **Gas atomisation:** For this method, aluminium in molten state is flame-sprayed on an porous spongy nickel-sheet. Afterwards, the plate is heated to initiate the forming of the Ni-Al alloy. To activate the catalyst the aluminium is leached of the metal sheet[32].
- **Mechanical alloying (MA):** MA is used to manufacture alloys with metastable phases. Therefore, the powder mixtures are processed by a ball mill at room temperature and under argon gas flow. Afterwards the aluminium is leached out with a KOH solution. One main advantage of the MA method is the reduced particle size, thus the higher surface area of the obtained alloy[33].
- **Melting:** The alloy is manufactured by melting together nickel and aluminium in a crucible followed by a quenching step. During quenching, different phases appear. Thus, the initial composition is substantial. The obtained phases react diverse to the leaching process and therefore, influence the porosity of the resulting material at a very high degree. The resulting metal is then grinded to a powder with the desired particle size.

3 Experimental

3.1 Preliminary Tests

Due to the fact, that the EBW-system is usually used for welding only, preliminary tests were carried out with melting of powdery material.

In the preliminary tests nickel and copper have been melted using Electron Beam Melting (EBM) into a homogeneous nugget to gather first experiences about the possibility of melting powders with this method [34].

After the first successful investigations, initial experiments were carried out to fuse nickel, aluminium, iron and chromium. The targeted composition was as follows:

	Ni	**Al**	**Fe**	**Cr**
[wt.%]	48	48	2	2

Two different crucibles were tested, one made of steel and the other one made of Titanium Zirconium Molybdenum-alloy (TZM). In both crucibles the same parameters were used, so one could investigate, whether there was a difference in the results caused by the pan materials or not. The parameters for this fusion processes are listed in Table 3.1.

Table 3.1: Melting steps of both samples. Constant parameters: U_B = 120 kV, f = 500 Hz, Figure = Spirale10000, A = 18 mm x 18 mm

Step	**I_B [mA]**	**t [s]**
1	2.4	26
2	2.6	26
3	2.6	26
4	2.6	30
5	2.6	28

Each sample was melted five times using the parameters listed in Table 3.1. Between the single melting steps, the nugget was turned upside down to ensure homogeneous alloying. Afterwards, the samples, which were prepared in different crucibles were characterised using Scanning Electron Microscopy (SEM). The close-up pictures and the corresponding SEM images can be seen in Figure 3.1.

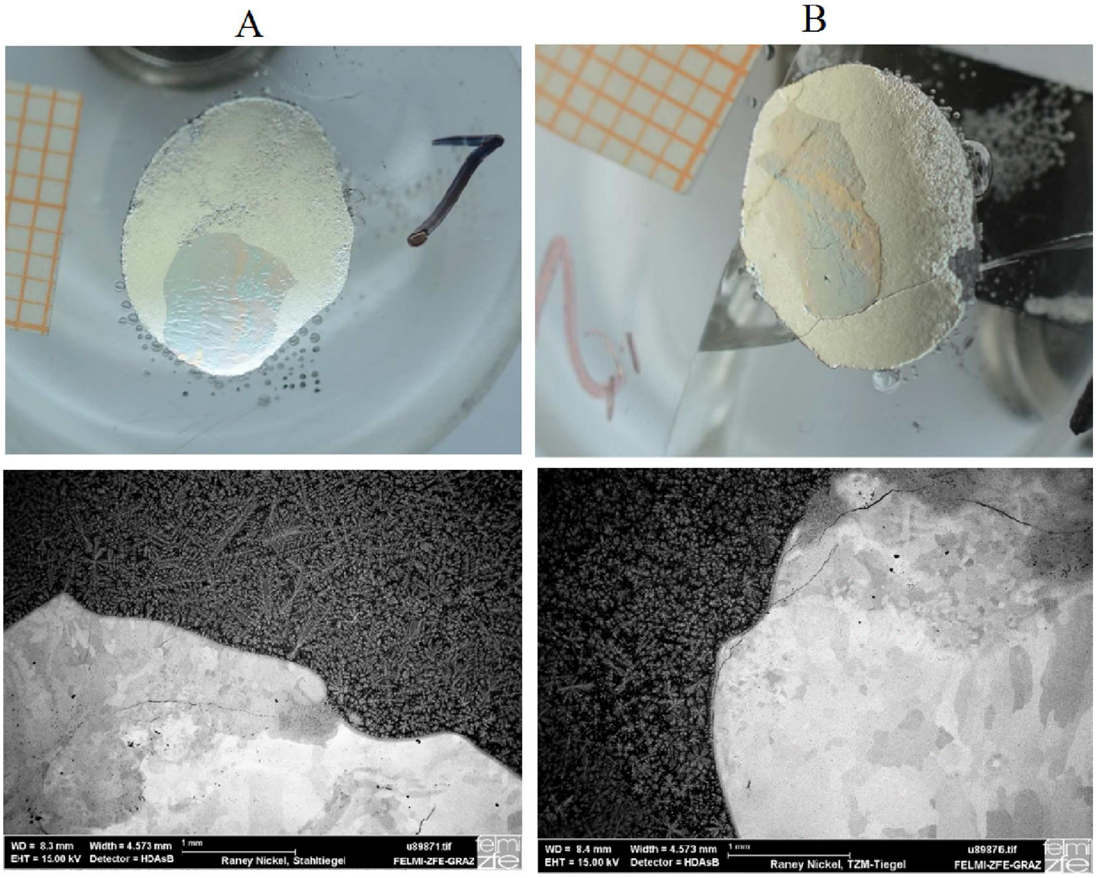

Figure 3.1: (a) Nugget manufactured in the steel crucible (left) and (b) in the TZM crucible (right) with the corresponding SEM-image.

No crucial difference between the two crucibles was detectable. Consequently, a more detailed analysis was performed with the nugget melted in the steel sample (Figure 3.1, A). Investigations with SEM made clear, there is a quite homogeneous alloy core, surrounded by a dendritical structure. The transition areas is shown in Figure 3.2.

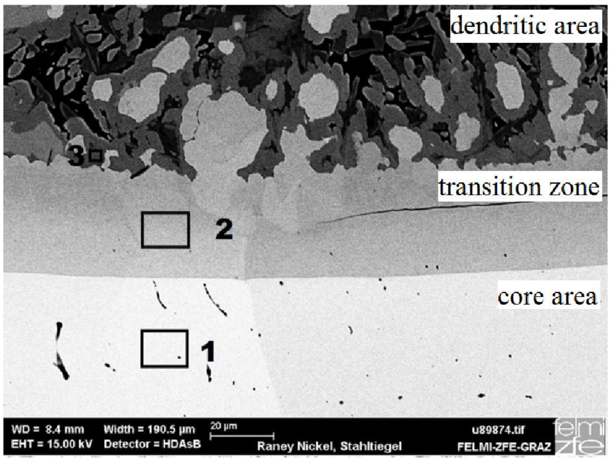

	Ni [wt.%]	Al [wt.%]	Fe [wt.%]
1	77.8	22.2	-
2	43.3	54.7	2.1

Figure 3.2: Transition area between homogeneous core and the dendritical structure and the corresponding elemental composition.

In both marked areas no chromium was detectable. Zone 1 consists of a very high nickel fraction whereas just half of the desired aluminium was left and none of the iron. Caused by the high fraction of nickel this zone appears brighter in the back scattered electrons (BSE) image. Compared to that, zone 2 differs from this composition. Apart from chromium, which was again not detectable, the other three elements were close to the targeted composition.

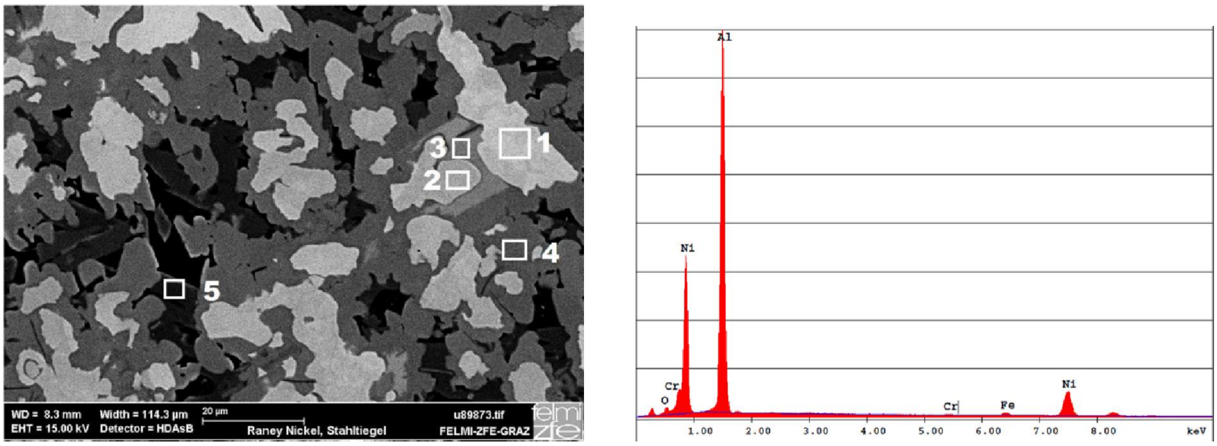

Figure 3.3: Dendritic structure: Five different areas for EDX analysis and the spectrum of the whole selected image section.

Table 3.2: Elemental composition of the five different areas in the dendritic section shown in Figure 3.3.

	Ni [wt.%]	**Al [wt.%]**	**Fe [wt.%]**	**Cr [wt.%]**
1	60.2	38.2	1.5	0.2
2	58.0	34.8	1.0	6.3
3	44.1	49.9	6.0	-
4	42.9	54.5	2.6	-
5	28.1	64.4	7.3	0.3

For more detailed information about the dendritic structure, energy dispersive X-ray spectroscopy (EDX) of five regions was performed (see Figure 3.3 and Table 3.2). Due to the different brightness of these areas in the BSE image, different chemical compositions were expected. In zone 1 and 2 the composition is close to the targeted one, although the aluminium content is slightly too low, whereas the nickel fraction is too high. Compared to that, zone 3 and 4 were close to the targeted composition but no chromium was detectable. In zone 5 the aluminium and iron fraction is elevated, but only 30 wt.% nickel remained.

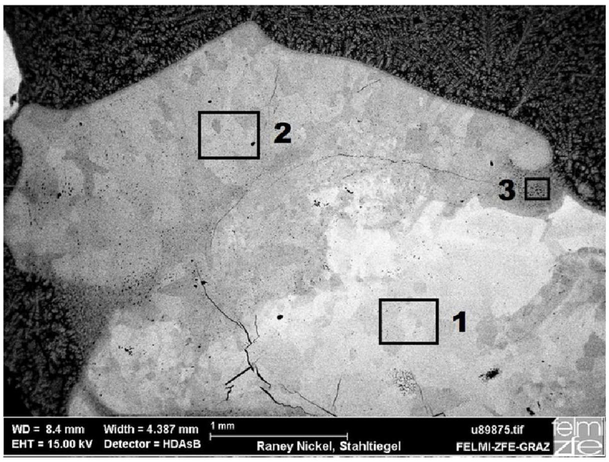

	Ni [wt.%]	Al [wt.%]	Fe [wt.%]
1	74.2	24.8	1.0
2	66.8	31.3	1.9
3	62.2	36.2	1.6

Figure 3.4: Homogeneous core with the elemental composition at three different areas.

Apart from the dendritic structure the nugget consists of a roughly homogeneous area arranged approximately in the center of the sample (Figure 3.1). One can clearly see a different brightness compared to the dendrites and therefore expect a deviating composition. None of the three chosen areas, marked in Figure 3.4, contains any chromium. The nickel content is elevated at the expense of aluminium. The iron content on the other hand is within the targeted range.

3.1.1 Results of the Preliminary Test

The experiments led to the conclusion, that both of the utilised crucibles are equally suitable. However, for subsequent tests the steel crucible was used. The obtained alloy was clearly subdivided into two different structures in terms of microstructure. Thus the main target was to adapt the preparation and the melting process in order to obtain a more homogeneous microstructure throughout the entire sample. In addition, the targeted alloy composition could not be reached during preliminary testing. Thus further optimisation of the melting process is required.

3.2 Experimental Set-up

3.2.1 Electron Beam Welding-System

The total view of the Electron Beam Welding-System (EBW) is shown in Figure 3.5. Basic technical specifications are listed in Table 3.3.

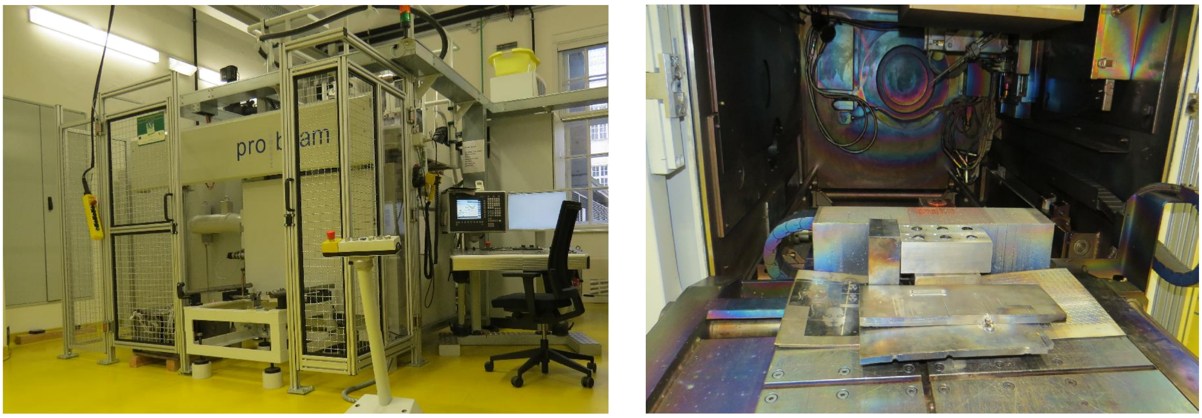

(a) (b)

Figure 3.5: (a) Total view of the EBW (TU Graz) and (b) inside the chamber.

Table 3.3: Key data of the ProBeam EBW-System [35,36].

Type	ProBeam EBG 45-150
Power, max.	45 kW
Acceleration voltage, max.	150 kV
Beam current	0.1 - 300 mA
Beam oscillation	$1^{\circ}.(\mu s)^{-1}$
Oscillation frequency, max.	1,000 kHz
Size of sample, max.	0.4 m x 0.4 m x 0.6 m
Velocity of table	0.5 - 1,000 $mm.s^{-1}$
Vacuum chamber	ca. 1.4 m^3
Evacuation time	$<$ 8 min
Pressure in chamber	$\leq 4 \times 10^{-3}$ mbar
Pressure in cathode column	$\leq 5 \times 10^{-5}$ mbar
Beam deflection	freely programmable

Apart from all the features mentioned in Table 3.3, it is also possible to melt steel workpieces up to a thickness of 120 mm within one layer. Filler wire can be used as well. An additional rotational and tilting device is also included.

3.2.2 Base Material

The base materials were purchased from Sigma-Aldrich and Alfa Aesar. They were only available in distinct shapes and grain sizes. Basic information as well as some images of the granulates and powders can be seen in Table 3.4 and Figure 3.6. A picture of the Raney®-Nickel powder that was used for some experiments is shown as well, however, further data were not provided. Iron was available in two different grain sizes, both of them are represented as well in Figure 3.6. Due to the easier distribution of the fine iron powder within the other materials, the coarser iron granulate was hardly ever used.

Table 3.4: Properties of the base materials: supplier, purity, form, molecular weight M, particle size D, boiling point T$_B$, melting point T$_M$ and density ρ [27,37]

	Ni	**Al**	**Cr**	**Fe**
Supplier	Sigma-Aldrich	Sigma-Aldrich	Alfa Aesar	Sigma-Aldrich
Purity [%]	99.7	99.7	99.99	99.99
Form	powder	granular	pieces	powder
M [g.mol^{-1}]	58.69	26.98	52.00	55.85
T$_B$ [°C]	2,732	2,460	2,672	2,750
T$_M$ [°C]	1,453	660	1,857	1,535
ρ [g.(mL)$^{-1}$]	8.9	2.7	7.14	7.86

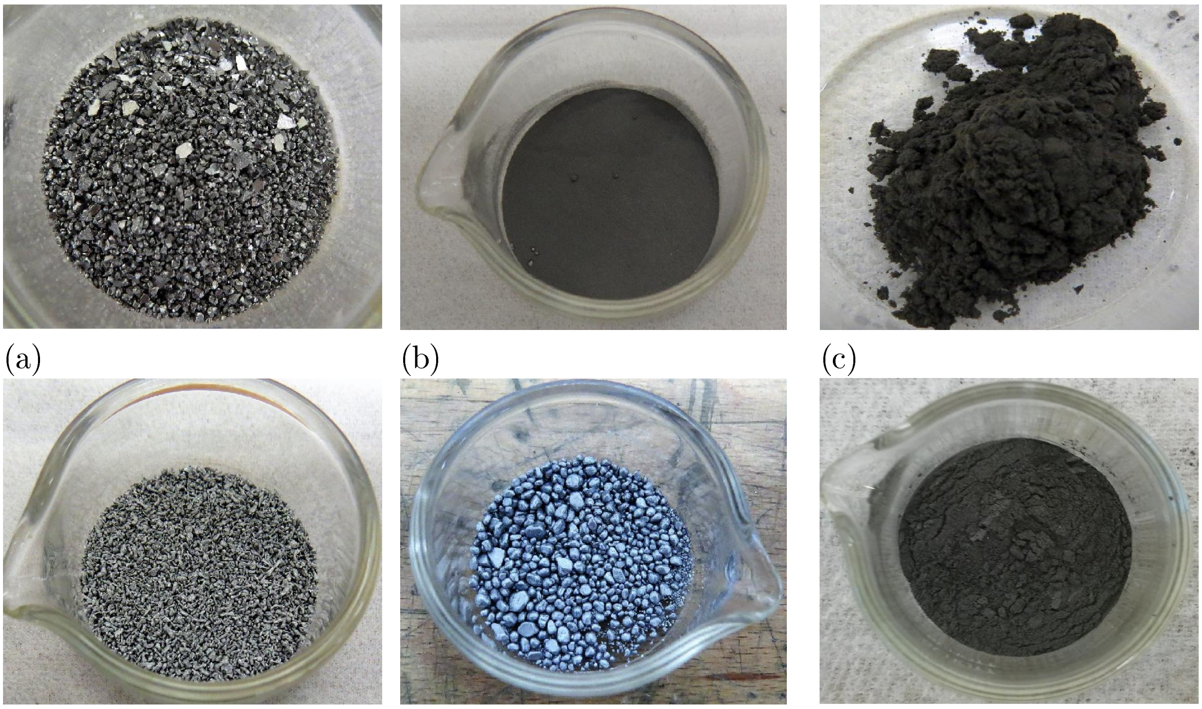

(a) (b) (c) (d) (e) (f)

Figure 3.6: (a) Iron, coarse granulate (b) iron, powder (c) nickel (d) aluminium (e) chromium (f) Raney®-Nickel.

3.2.3 Crucible

At the beginning bigger crucibles were manufactured to facilitate the experiments and to obtain bigger alloy nuggets. Therefore, a square profile of construction steel S 235 JR was cut into the desired dimensions of 150 mm x 40 mm x 50 mm with a circular saw. Three cavities with a diameter of 20 mm and a depth of 24 mm were drilled into the block using the *Optimill MB4* unit and a *HSS twist drill*. As a cooling lubricant an oil-water emulsion was utilised. On the reverse side three cavities with a diameter of 30 mm and 12 mm depth were manufactured. In the course of the first experiments it turned out that the crucibles with higher depth were more suitable.

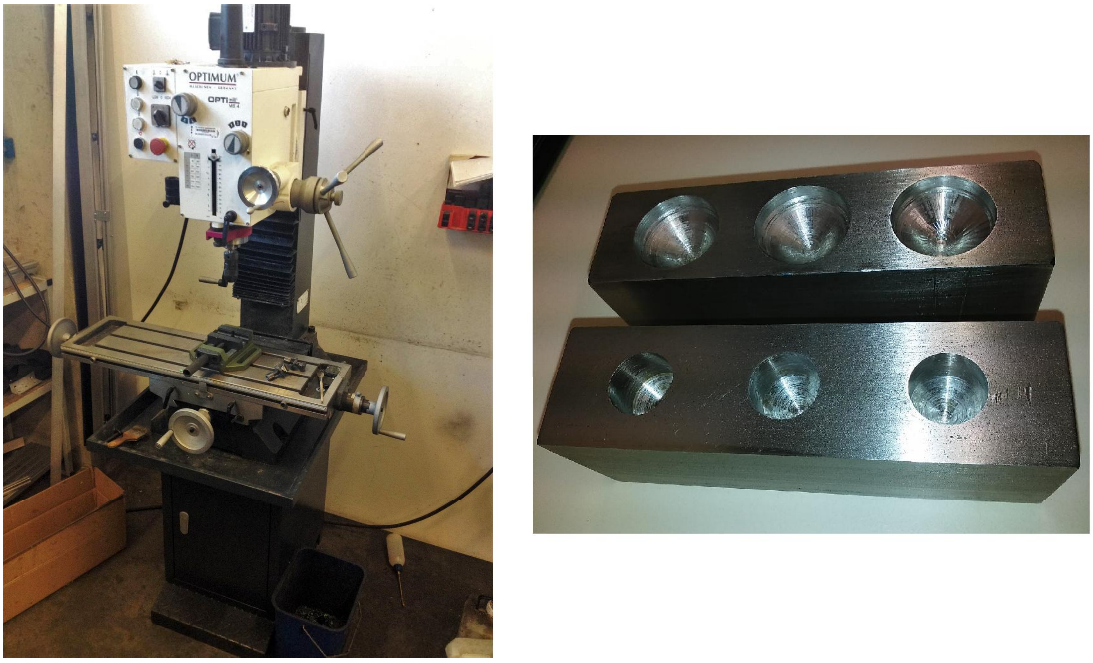

Figure 3.7: Drilling machine and manufactured crucibles.

3.3 Preparation

3.3.1 Sample Preparation

For the following investigations, the Institute of Chemical Engineering and Environmental Technology (CEET) provided the material for all the experiments. As one can see in Figure 3.6 the grain sizes vary widely among the different metal powders.

Nickel and Raney®-Nickel have only been available as powdery particles, whereas aluminium was apparently coarsely granular. Two different grain sizes for iron were available, one was a fine powder similar to nickel, the other one was comparable in terms of particle size to Al. To gain some information about a possible difference in the behaviour of these powders during the melting process, both of them were used to compare the results. The purchased Cr consisted of plates with a broad range of distinct sizes up to 1 cm. Therefore, it was necessary to machine it in advance with a mortar and afterwards grind it in an eccentric ball-mill. These processes were carried out at the Institute for Chemistry and Technology of Materials (ICTM) by Prof. Reichmann. After grinding a smaller variation in the grain sizes was obtained, which facilitated the uniform distribution of all the materials by manual stirring. This is specifically important for dispersing the small amounts of Fe (2 wt.%) and Cr (2 wt.%) within the starting material powder.

Figure 3.8: (a) Chromium, as purchased and (b) chromium, after milling.

3.3.2 Preparation of Experiments

At the beginning of all melting experiments the steel crucible had to be demagnetised by using the (*wagner magnete 211-17/40 S-1*) demagnetiser in order to avoid deflections of the electron beam. Apart from that, it was necessary to remove the impurities and possible sediments with a wire brush. Subsequently, it was cleaned by compressed air and isopropanol.

Figure 3.9: Demagnetiser *wagner magnete 211-17/40 S-1*

The powders were weighed precisely into a glass pan and mixed manually, before putting the mixture in the crucible. For the following tasks a minimum mass of 4 g was required to get reasonable results.

When handling all these materials it was crucial to take protective measures such as gloves to avoid direct contact with the powders, since some might cause allergic skin reactions. Also one should avoid to inhale the dust by wearing a respirator, particularly when using nickel powder due to the fact that nickel oxide is toxic.

Inside the chamber steel sheets were placed beneath the pans as precaution for the very unlikely case of melting the steel crucible. Apart from that, another sheet metal was positioned right in front of the air stream ensuring that the powders will not be blown away when floating the chamber.

After arranging the metal sheets, the pans were positioned inside the chamber right next to the copper block, on which the electron beam is focused.

If a sample is melted several times, the removal of excess powder after the first melting step is required. Otherwise it would possibly interfere with the following melting processes in terms of uneven heat conduction. When all powder is removed, the alloy nugget is directly in contact with the steel pan enabling a uniform, thus more effective heating.

4 Results and Discussion

4.1 Floating Tests

Initial floating tests were performed in order to quantify the drag-out, if any, of the fine powder materials during evacuation of the EBW-chamber. For this purpose a certain amount of powder was placed in the crucible and the total mass was weighed and placed in the EBW unit. Afterwards the chamber was evacuated. After venting, the total weight of the crucible with the powder was weighed again to determine the total mass loss. The results of these tests can be seen in Table 4.1.

Table 4.1: Mass change of the different base materials

	Ni	**Al**	**Fe**
m_{start} [g]	0.48	0.50	0.53
m_{float} [g]	0.44	0.49	0.52
m_{loss} [g]	0.04	0.01	0.01
m_{loss} [%]	8	2	2

The calculated mass loss did not exceed 8%, hence the weight loss caused by floating of the chamber was assumed to be negligible. Due to the fact that the losses for Ni were the highest, an eye was kept on the resulting Ni content in the alloy after melting. Apart from possible losses caused by floating, further losses could appear during the melting processes depending on the chosen parameters.

4.2 Melting

After the floating tests, the first fusion experiments were performed using the parameters from preliminary testing. However, it must be taken into consideration, that the base material provided for the following tasks was different from the previous ones. For this reason the results are only comparable to the pretests to a certain extent.

At the beginning the former crucibles were used, but could not carry the targeted 4 g total mass of powder. Thus new crucibles with higher capacities were manufactured as mentioned above.

Initially a Raney®-Nickel powder from Alfa Aeser was melted followed by fusion tests with nickel and aluminium. After optimisation of several process parameter, such as current and frequency, Ni, Al, Fe and Cr were simultaneously subjected to melting.

In Table 4.2 the EBW parameters and the corresponding abbreviations that are used for all of the fusion tests are listed.

Table 4.2: Abstract of the accessible EBW parameters for melting of the metal powders.

U_A	acceleration voltage	[kV]
I_B	beam current	[mA]
A	beam amplitude	[mm]
t_b	impact time	[s]
Figure	beam figure	
f	frequency	[Hz]

4.2.1 Raney®-Nickel

As mentioned before, at the beginning of this thesis experiments were performed with melting a commercial Al-Ni alloy (Raney®-Nickel from Alfa Aesar) with an Al to Ni ratio of 50/50. The idea was to investigate the melting behaviour of this alloy. In case of a good weldability the targeted amount of iron and chromium could be added to the commercial Al-Ni powder. Thereby the number of different powders that had to be fused, could have been reduced from four to three. Naturally, this would facilitate the manufacturing and the preparation of the final alloy. It must be noted that the processing of the Raney®-Ni powder is dangerous to health. Especially the dust is toxic, thus an adequate dust mask is essential, gloves are compulsory in any case. The melting process is shown step by step in Figure 4.1.

Table 4.3: EBW parameters for melting of Raney®-Ni.

U_A [kV]	**I_B [mA]**	**A [mm]**	**t_B [s]**	**f [Hz]**	**Figure**	**m_{start} [g]**
120	3.0	19 x 19	20	1,000	Spirale10000	4.00

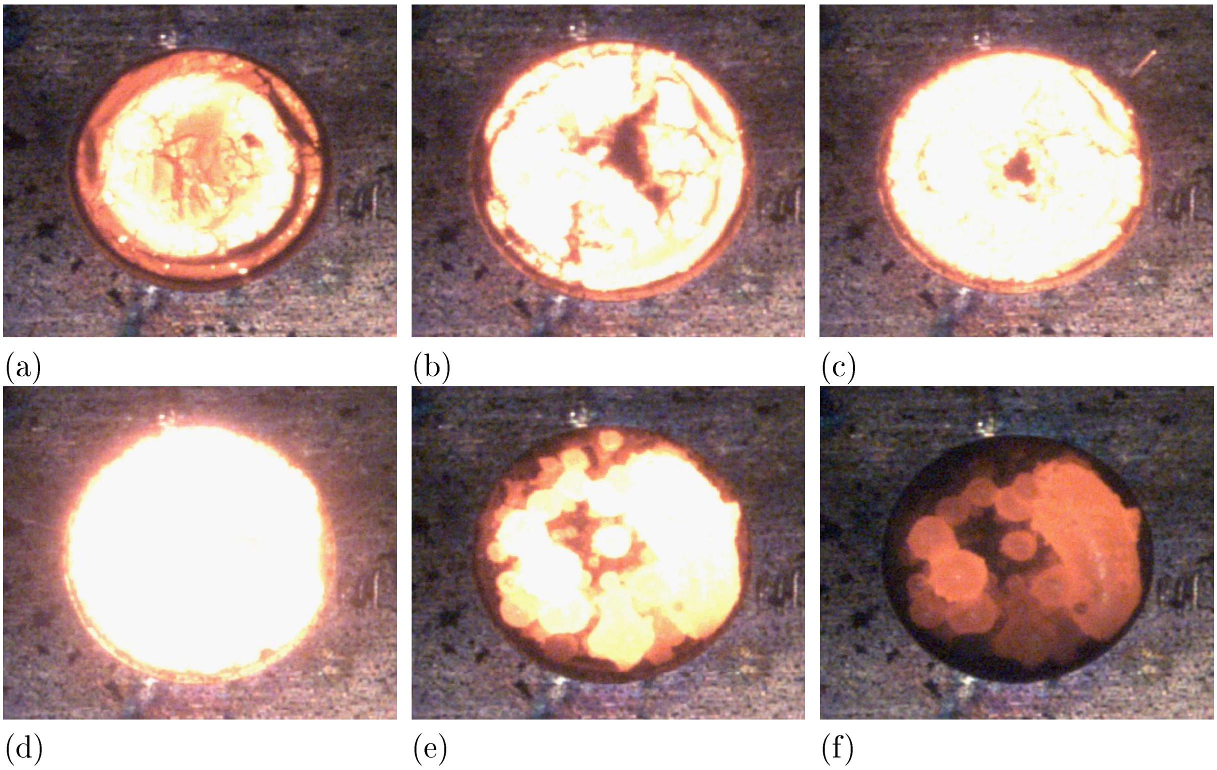
(a) (b) (c) (d) (e) (f)

Figure 4.1: Different steps of the melting process of Raney®-Nickel powder after (a) 1 s (b) 2 s (c) 3 s (d) 4 s (e) 14 s (f) 19 s.

After 1 s of melting the major part of the powder already started to ignite (a). 3 s later the whole mass was melted (d) and solidified after 14 s (e-f). Although it looked like the material was melted homogeneously, many grains were generated, instead of forming only one single nugget. One can assume that the powder is inhomogeneous and not suitable for this purpose. Since the melting experiments with the base material showed more promising results, the Ni-Al powder was not used for further investigation.

4.2.2 Ni-Al

After the initial melting experiments of the commercial Ni-Al alloy powder, the fusion of Ni and Al powders was investigated, in order to find the ideal process parameters.

For this experiments $m_{Ni} = 2.03$ g and $m_{Al} = 2.04$ g were fused using the following parameters in Table 4.4.

Table 4.4: EBW parameters for the first and second melting cycle.

U_A [kV]	I_B [mA]	A [mm]	t_B [s]	f [Hz]	Figure	m_{start} [g]	m_{final} [g]
120	3.00	19 x 19	40	500	Spirale10000	4.07	3.58

The first melting cycle of this alloy can be seen in Figure 4.2. The fusion as well as the solidification is displayed step by step. During the process the different powder grains melt and form a spheroidal structure due to surface tension. The nugget was shaped within around 6-8 s. The remaining processing provides a heat treatment, where the elements distribute evenly throughout the sample.

According to Figure 2.12 the phases Al_3Ni (T_{melt} = 854 °C) and Al_3Ni_2 (T_{melt} = 1133 °C) mainly build up at this composition. After formation of the alloy nugget, it will not be remelted by the electron beam with the same energy due to the higher average melting point of the nugget alloy.

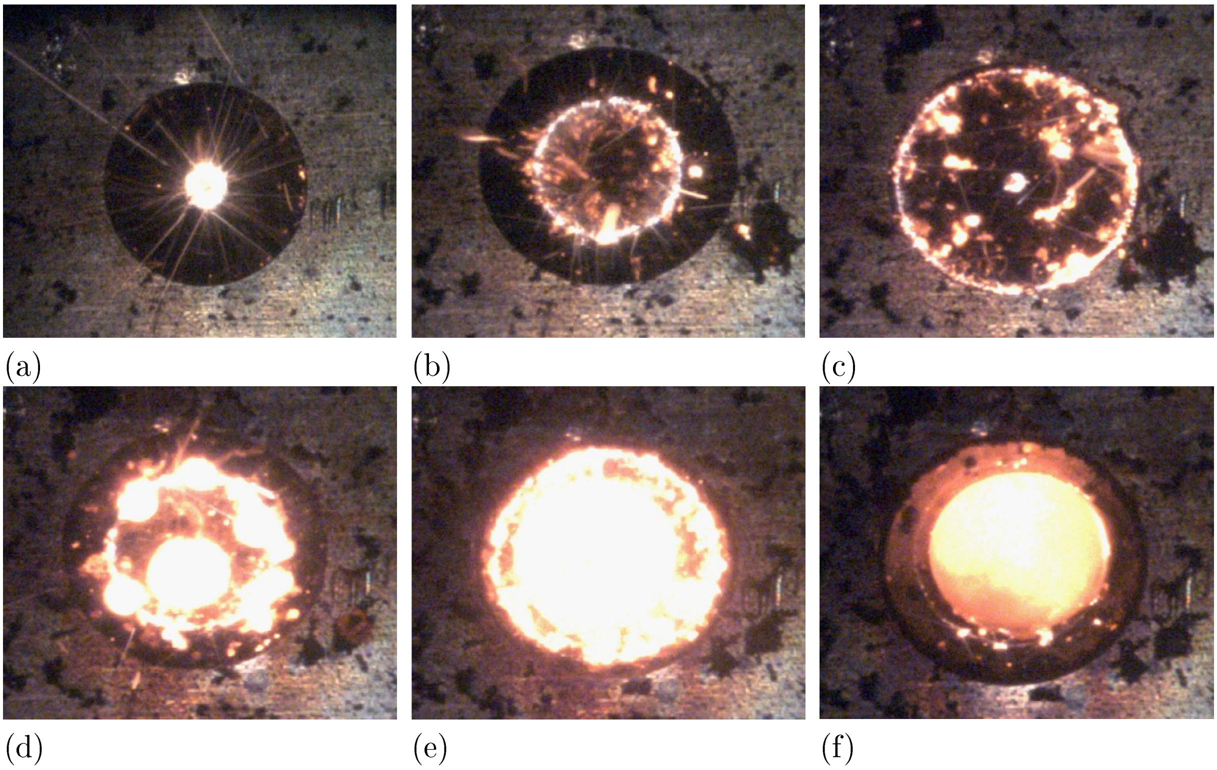
(a) (b) (c)
(d) (e) (f)

Figure 4.2: Different steps of the first melting cycle of Ni and Al after (a)-(c) 1 s (d) 2 s (e) 4 s (f) 6 s.

After the first melting step the excessive material left in the crucible was removed. The nugget was tilted so that the bottom side could be targeted by the electron beam. The second melting cycle was mainly performed for further homogenisation of the nugget. Figure 4.3 shows this process. There is a clear difference between the first and the second melting cycle (compare Figure 4.2 and Figure 4.3). After formation of the alloy nugget, it only incandescence and gets a smoother surface.

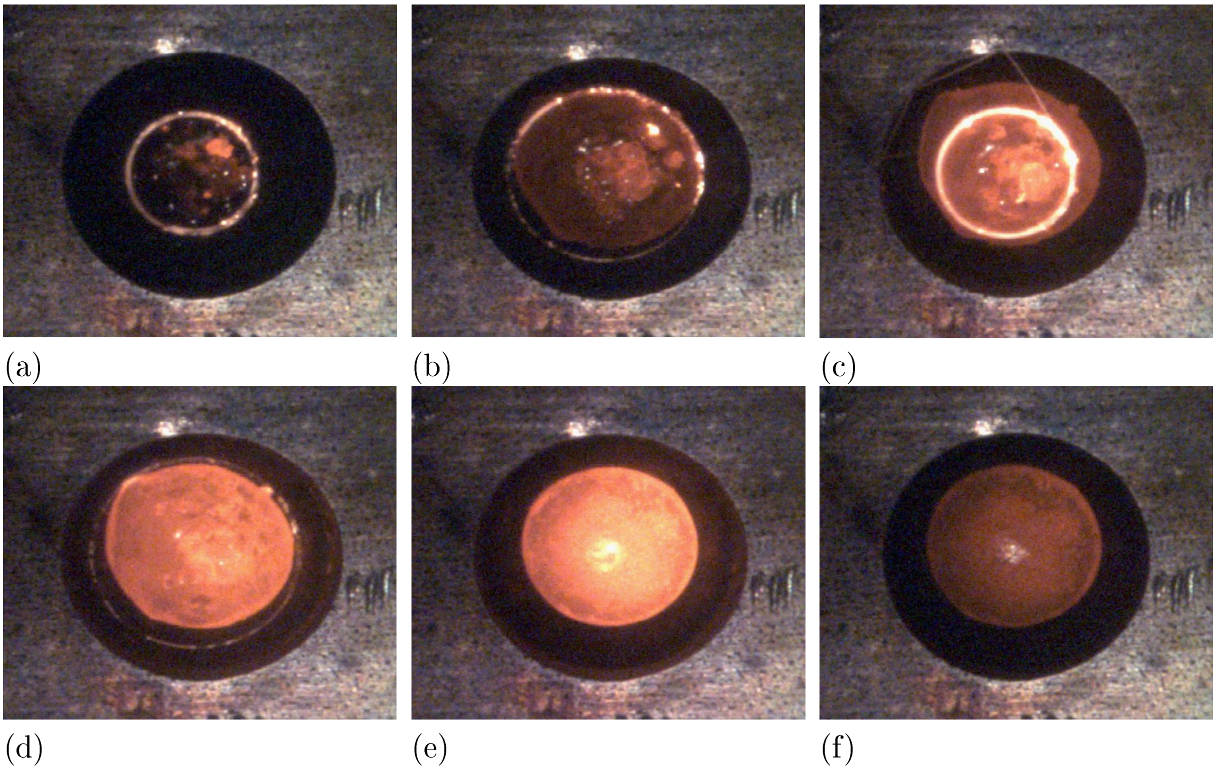

Figure 4.3: Different steps of the second melting cycle of the same NiAl nugget after (a) 7 s (b) 11 s (c) 12 s (d) 14 s (e) 19 s (f) 22 s.

The front and the back side of the resulting nugget after these two cycles can be seen in Figure 4.4. The final mass is 3.58 g and the estimated diameter 14.2 mm.

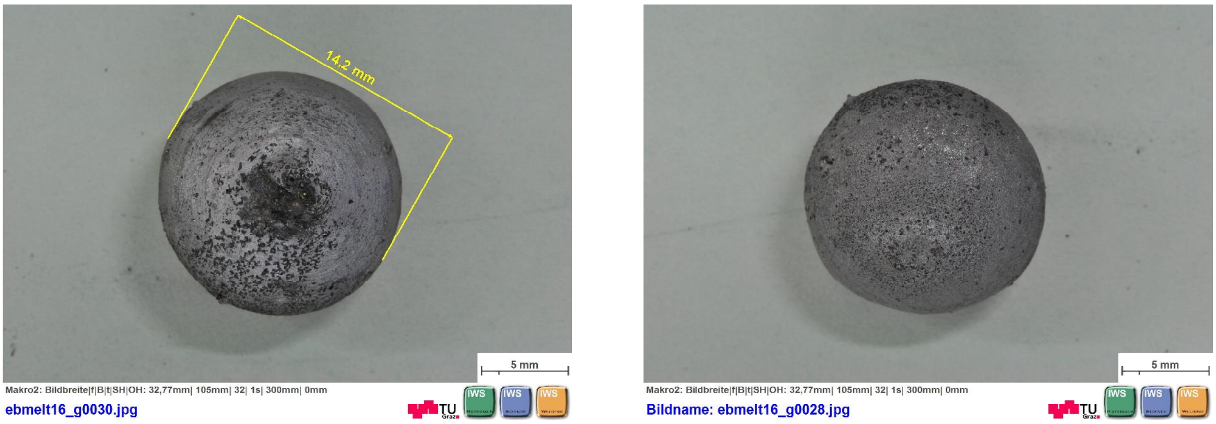

Figure 4.4: Front and back side of the NiAl nugget manufactured in two steps.

Subsequently the Ni-Al nugget was cut in half, cold mounted in epoxy raisin, grinded and polished to enable investigations of the cross section using light microscopy. The results are shown in Figure 4.5.

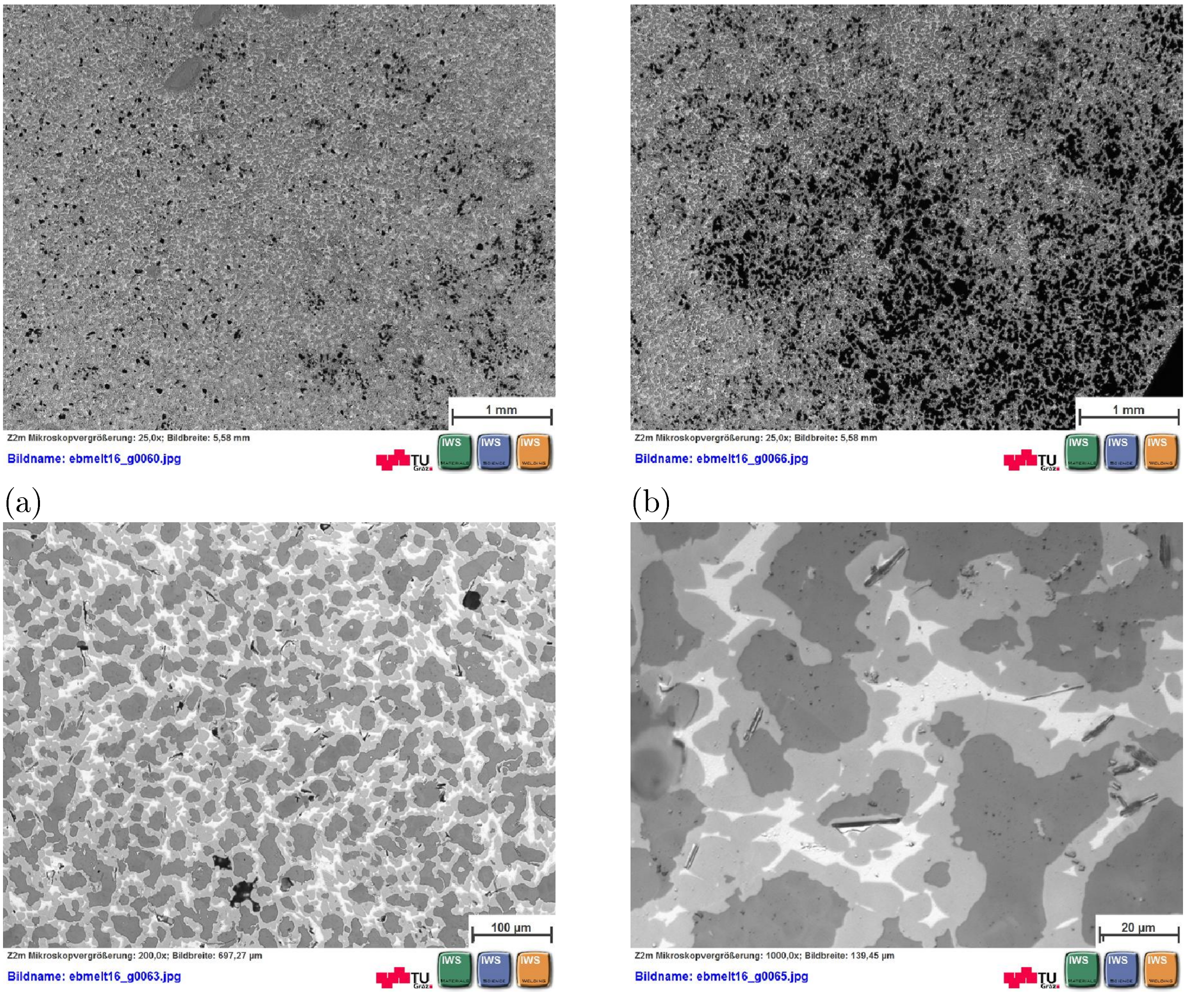

(a) (b)

(c) (d)

Figure 4.5: Different sections of the Ni-Al alloy (a) homogeneous distribution of Ni and Al, (b) high porosity, especially in the surface zone (c) microstructure at higher magnification, (d) three different phases are visible.

The microstructure is quite homogeneous, although porosities are obtained throughout the entire alloy sample, specifically near the surface of the nugget (Figure 4.5). Three phases are visible at higher magnification. EDX-analysis was performed additionally to get information about the phases (Figure 4.6). It is uncertain, whether the three areas represent different phases or segregations. However, due to the diverse chemical composition, it is assumed, that these are phases.

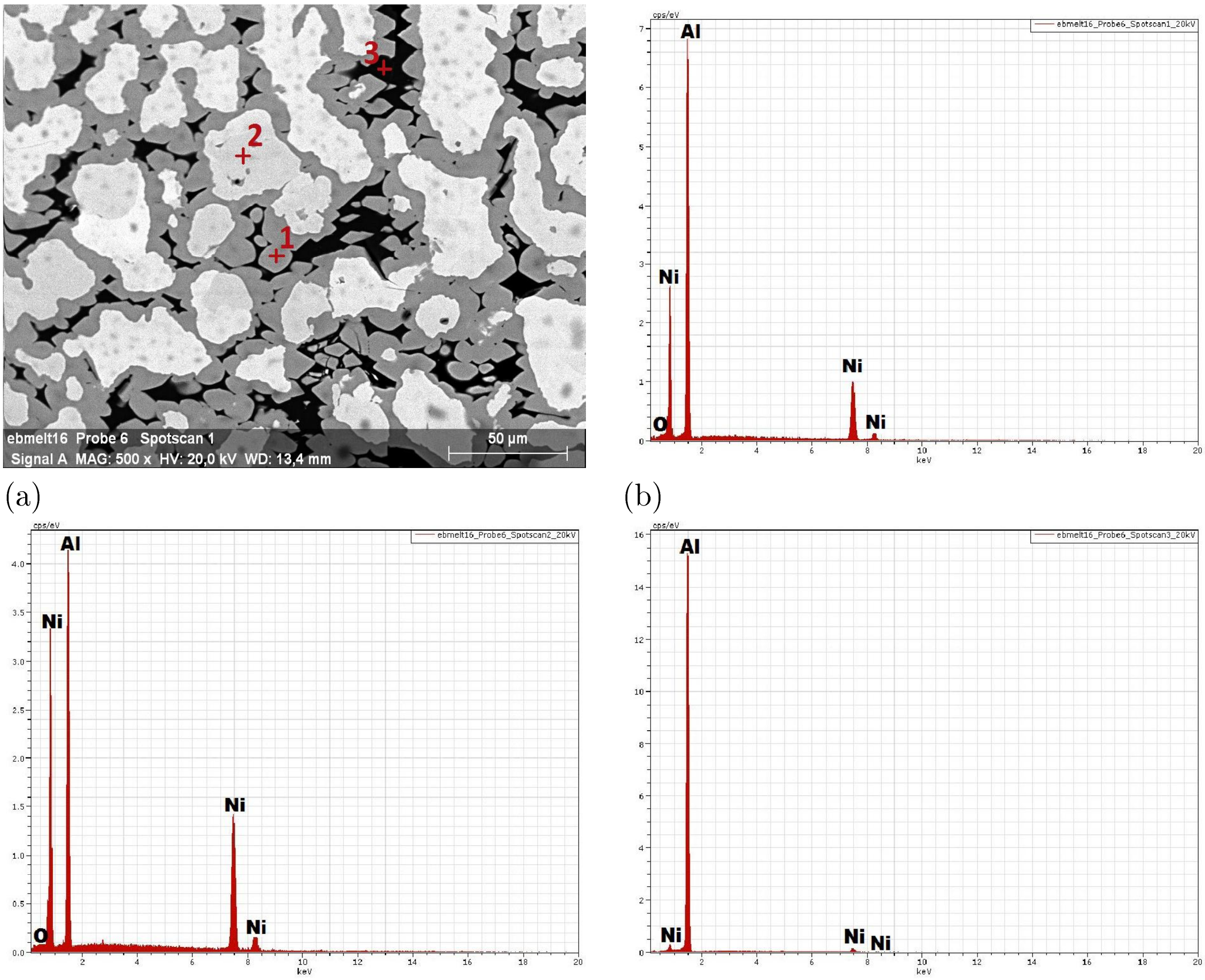

(a) (b) (c) (d)

Figure 4.6: EDX-analysis of the three different phases (a) BSE-image (b) spot-scan 1 (c) spot-scan 2 (d) spot-scan 3.

Spot-scan 1 shows a Ni to Al ratio of 50/50. In spot-scan 2 the Ni fraction is slightly elevated at the expense of Al. However, in spot-scan 3 no Ni is detectable. Thus, Phase 3 only consists of Al. When comparing the compositions of the different spot-scans, it is substantial to keep in mind, that in all plots the scalings of the y-axis is different.

Microhardness Measurement HV

For further investigations of the phases, microhardness measurements were performed (Figure 4.7). Due to the high porosity of the nugget, the microhardness could not be determined exactly. Thus, a high measuring inaccuracy is obtained.

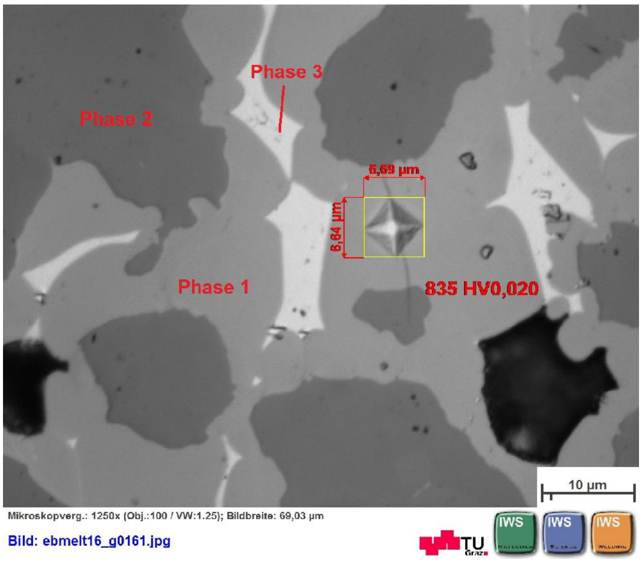

	HV0.020
Phase 1	832 ± 46
Phase 2	1,023 ± 59
Phase 3	n/a

Figure 4.7: Vickers microhardness measurements of the three phases marked in the left image.

The microhardness of Phase 3 cannot be measured, due to its small size. However, an upper limit is estimated. In addition, Phase 2 is apparently very brittle. Thus, cracks occurred during the measurement, influencing the obtained values as well. The values in the Table above (Figure 4.7) show very high hardness of Phase 1 and 2. When combining the information from EDX-spectra (Figure 4.6) with the one obtained from hardness measurements, the phases can be identified using the Ni-Al phase diagram (Figure 2.12). According to hardness values for this phases in literature (759±25 HV) and the composition from EDX-analysis, Phase 1 is referred to Ni_2Al_3. Phase 3 is obviously almost pure Al, which agrees with results found in literature (Al: 21-48 HV) [38]. When comparing the composition of Phase 2 with the one appearing in the Ni-Al phase diagram, it can be assumed, that due to the high Ni content, Phase 2 mainly consists of $AlNi_3$. No microhardness could be found in literature for this phase.

Comparison of different frequencies

To investigate the influence of the diverse melting parameters further experiments were performed with Al and Ni powder, using different frequencies. Previous tests showed that f = 500 Hz is sufficient. However, the following frequencies were additionally tested: 50 Hz, 1,000 Hz, 2,000 Hz, 3,000 Hz and 5,000 Hz. The resulting nuggets are listed in Figure 4.8.

Table 4.5: EBW parameters for the test series with different frequencies.

U_A [kV]	I_B [mA]	A [mm]	t_B [s]	f [Hz]	Figure
120	3.00	19 x 19	40	50 - 5,000	Spirale10000

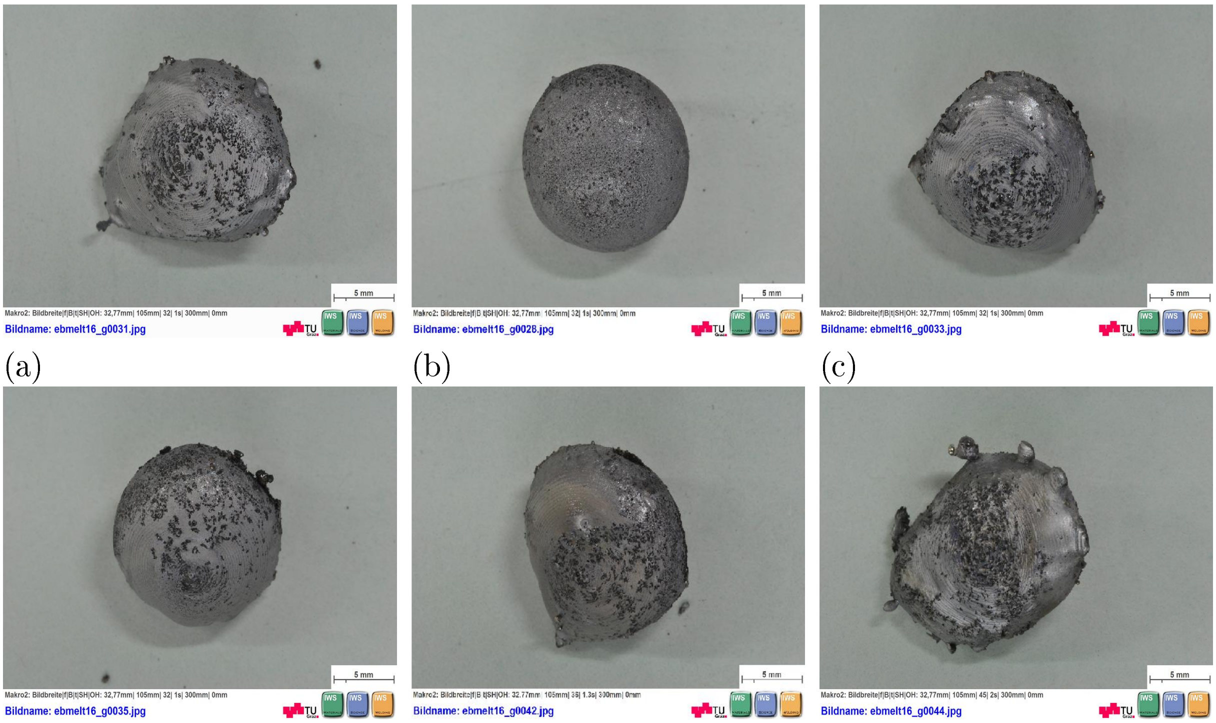

(a) (b) (c)

(d) (e) (f)

Figure 4.8: Results of melting with different frequencies (a) 50 Hz (b) 500 Hz (c) 1,000 Hz (d) 2,000 Hz (e) 3,000 Hz (f) 5,000 Hz.

By changing the frequency from 50 Hz to 500 Hz the result is improving. Further elevation to 1,000 Hz and especially to 2,000 Hz result in a nugget that is macroscopic more uniform. Above a frequency of 3,000 Hz there is no further improvement. The nugget melted using 5,000 Hz shows a completely irregular shape, thus no additional tests with higher frequencies were performed. It has to be mentioned, that the nugget in Figure 4.8 (b) fused with 500 Hz was melted twice, thus it cannot be compared directly to the other results.

Table 4.6: Different frequencies and the corresponding mass loss during the melting process.

	a	**b**	**c**	**d**	**e**	**f**
f [Hz]	50	500	1,000	2,000	3,000	5,000
m_{start} [g]	4.05	4.07	4.06	4.09	4.01	4.10
m_{final} [g]	3.51	3.58	3.44	3.40	3.49	3.55
m_{loss} [g]	0.54	0.49	0.62	0.69	0.52	0.55

As can be seen in Table 4.6, the mass loss is not influenced by varying frequencies.

Comparison of different beam currents

Subsequently, another experimental series was carried out to investigate the influence of different beam currents. The tests were started with a current of 1.8 mA and then increased stepwise by 0.2 mA. Previous tests already used a current of 2.8 mA, thus it was not repeated.

Table 4.7: EBW parameters for the test series with different beam currents.

U_A [kV]	**I_B [mA]**	**A [mm]**	**t_B [s]**	**f [Hz]**	**Figure**
120	1.8 - 3.0	19 x 19	40	1,000	Spirale10000

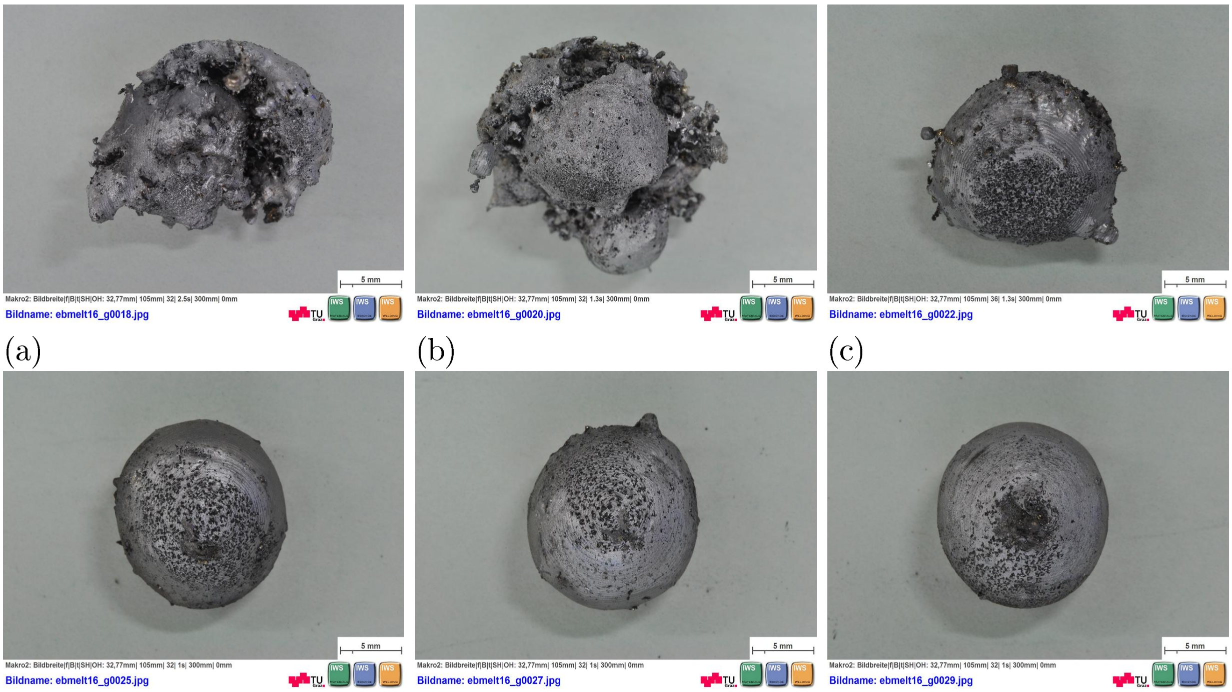

(a) (b) (c)

(d) (e) (f)

Figure 4.9: Results of applying different beam currents: (a) 1.8 mA (b) 2.0 mA (c) 2.2 mA (d) 2.4 mA (e) 2.6 mA (f) 3.0 mA.

Figure 4.9 shows nuggets formed using six different beam currents. The melting processes using 1.8 mA and 2.0 mA resulted in misshapen nuggets, as a spheroidal shape is hardly visible. It can be assumed, that at this low currents the energy input was not high enough. An improvement concerning the shape was obtained by increasing the current to 2.2 mA. With a beam current of 2.4 mA and 2.6 mA further uniforming of the nuggets is recognisable. From macroscopic point a current of 3.0 mA gave the best results after one melting step. The alloy nugget had a clearly round shape and smooth surface compared to the nuggets melted with lower currents. Due to increasing uniformity of the nugget with higher beam currents, following tests were carried out using currents between 2.4 - 3.0 mA.

Table 4.8: Different currents used for the six samples and the corresponding mass losses

	a	**b**	**c**	**d**	**e**	**f**
I [mA]	1.8	2.0	2.2	2.4	2.6	3.0
m$_{start}$ **[g]**	4.05	4.03	4.05	3.99	4.05	4.07
m$_{final}$ **[g]**	3.78	4.01	3.67	3.56	3.49	3.58
m$_{loss}$ **[g]**	0.27	0.02	0.38	0.43	0.56	0.49

According to Table 4.8, the mass loss is influenced by varying currents.

Mass losses during processing

For both test series the mass of the base materials before and the mass of the resulting nugget was recorded. The calculated mass losses depending on frequency and current are shown in Figure 4.10.

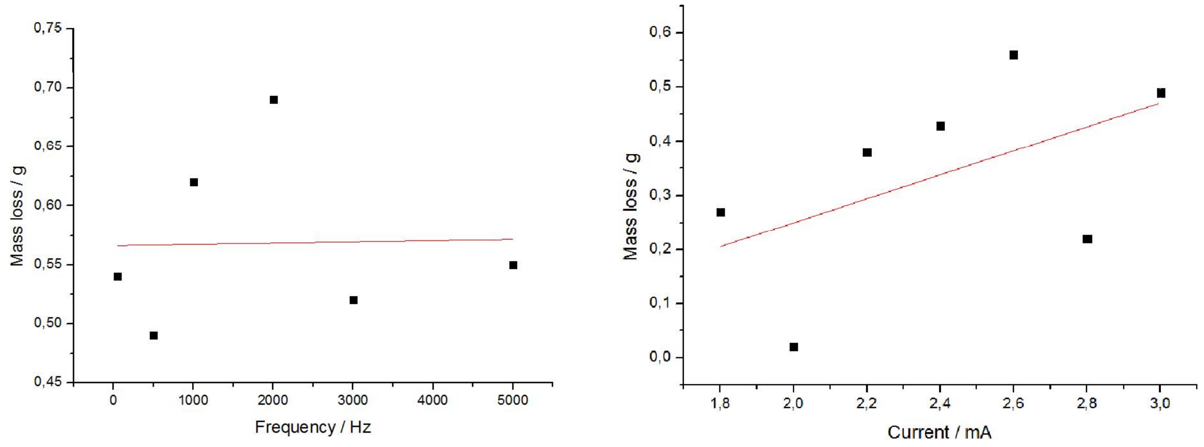

Figure 4.10: Mass loss depending on different frequencies and currents

A linear fit was applied to both plots in order to show, if a correlation between increasing f or I and Δm is detectable. According to graphs in Figure 4.10, no trend of the mass loss is observable throughout the complete investigated frequency range.

However, the mass loss increases with increasing currents, due to the higher energy input. This aspect should be taken in consideration when choosing a certain beam current.

4.2.3 Ni-Al-Fe-Cr

The melting of Ni and Al delivered useful information regarding the optimum ranges of processing parameters for subsequent testing. Ni (m_{Ni} = 2.03 g), Al (m_{Al} = 2.04 g), Fe (m_{Fe} = 0.14 g) and Cr (m_{Cr} = 0.10 g) were fused using the following parameters:

Table 4.9: EBW parameters for melting Ni, Al, Fe and Cr.

U_A [kV]	I_B [mA]	A [mm]	t_B [s]	f [Hz]	Figure	m_{start} [g]	m_{final} [g]
120	3.00	19 x 19	40	1,000	Spirale10000	4.26	3.73

The melting process is imaged step by step in Figure 4.11. It looks quite similar to the fusion of only Ni and Al in Figure 4.2. After only 1 s minor spheroids were already formed (a) and joined to bigger spheres within 3 s (b). After 5 s they agglomerated, thus all the small grains were absorbed into one large sphere (c).

Afterwards the electron beam was used for the the heat treatment of the already shaped nugget (d)-(f).

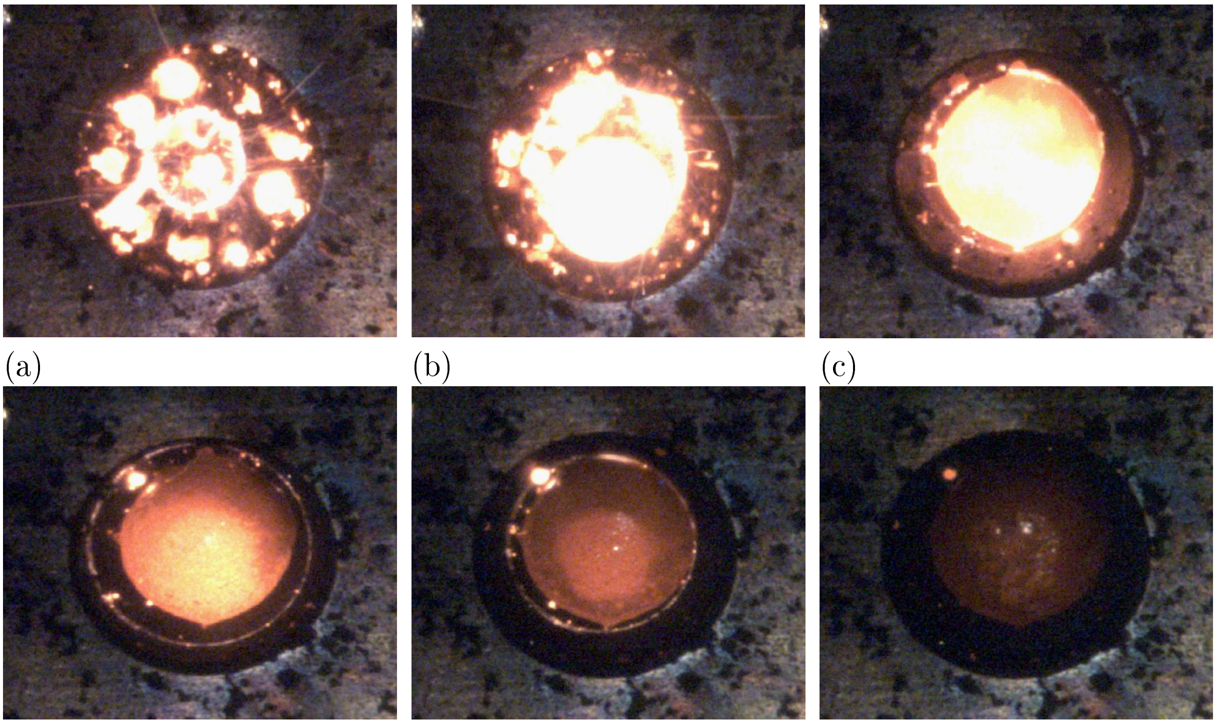
(a) (b) (c)
(d) (e) (f)

Figure 4.11: Different steps of the first melting cycle of Ni, Al, Fe and Cr after (a) 1 s (b) 3 s (c) 5 s (d) 7 s (e) 10 s (f) 20 s.

Front and back side of the alloy nugget manufactured in one melting cycle is shown in Figure 4.12.

Figure 4.12: Front and back side of the Ni-Al-Fe-Cr nugget melted in one step.

For further analysis, the nugget was cut in half, cold mounted in epoxy raisin, grinded and polished. Afterwards, the surface was investigated using light microscopy (Figure 4.13).

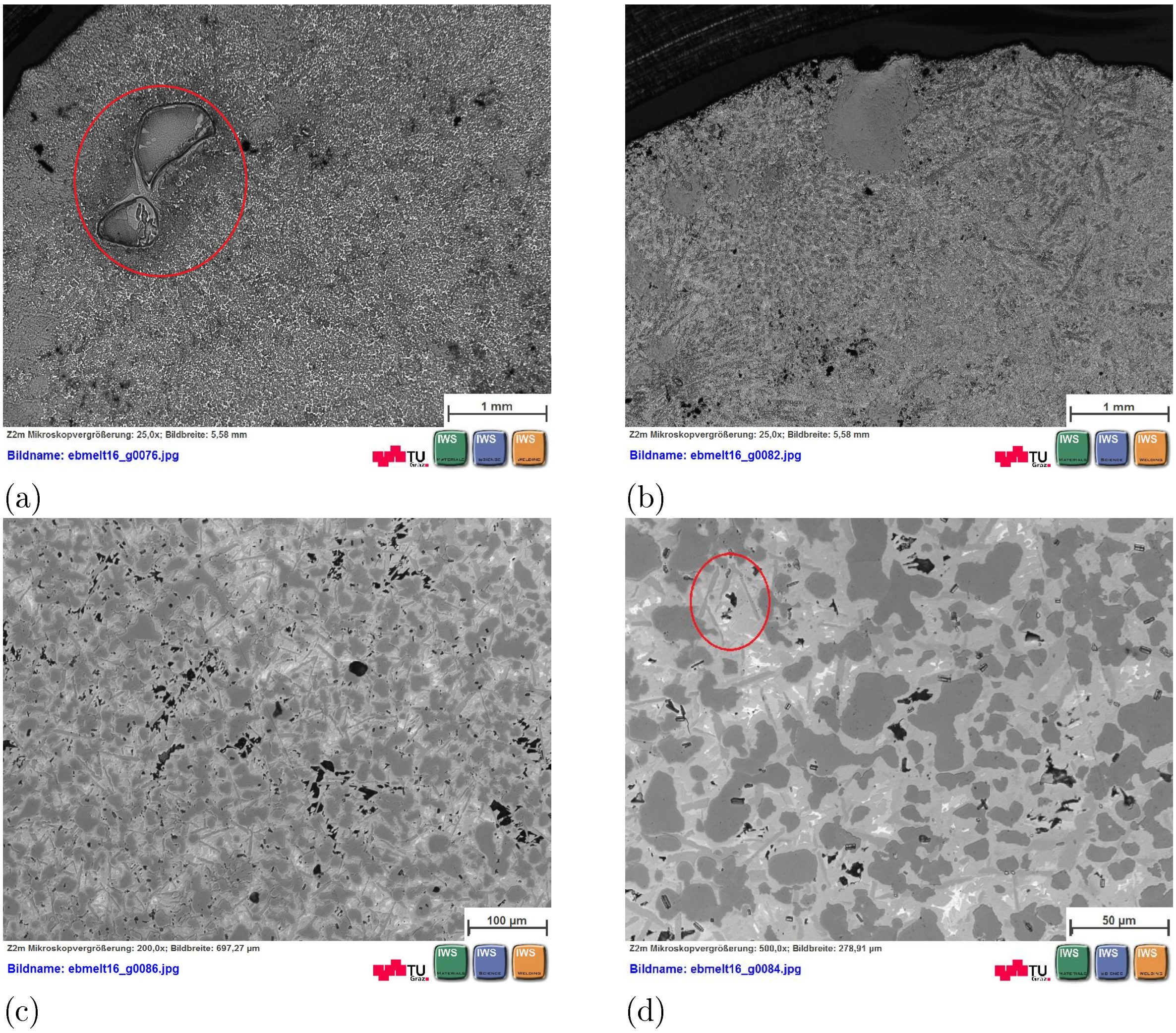

(a) (b) (c) (d)

Figure 4.13: Different microstructure images of the Ni-Al-Fe-Cr nugget alloy (a)-(b) segregations in the near-surface areas (c) pores in the centre of the nugget (d) three phases are observable at higher magnification.

According to the images in Figure 4.13, the microstructure is fine granular with needle-like structures (d). It is mainly homogeneous, however, some segregations are observable, especially near the surface (a). Again, some pores spread throughout the whole sample. At higher magnification three different phases can be identified. Further investigations were performed using SEM and EDX-analysis. It is uncertain, whether the three areas represent different phases or segregations. However, due to the diverse chemical composition, it is assumed, that these are phases.

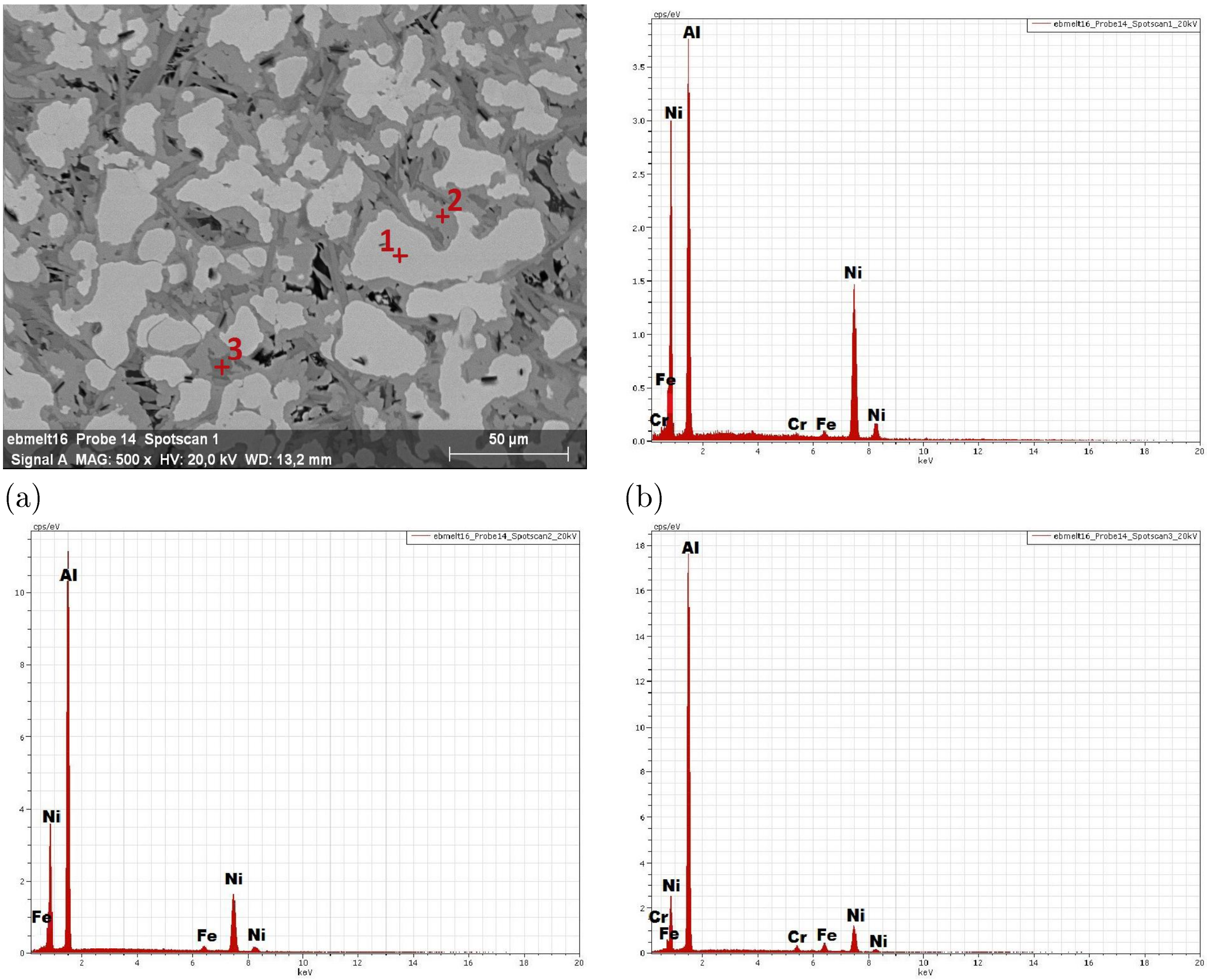

(a) (b)

(c) (d)

Figure 4.14: EDX-analysis of the three different phases (a) BSE-image (b) spot-scan 1 (c) spot-scan 2 (d) spot-scan 3.

When comparing the compositions of the different spot-scans (Figure 4.14), it is substantial to keep in mind, that in all plots the scalings of the y-axis is different. These scans show diverse compositions of the microstructure. In spot-scan 1 the Ni-content is higher than the Al-content. Spot-scan 2 shows a higher Al-fraction at the expense of Ni. In spot-scan 2 the Al-content is even twice as high as the Ni-content. Fe and Cr is detectable in area 1 and 3, but area 2 shows no Cr-content.

Elemental Mapping

The BSE images exposed some inhomogeneities, thus, elemental mapping was used to analyse one representative spot in particular. With this method it was possible to display the element distribution of the sample surface.

The following Figure 4.15 shows one of the conglomerates. It is obvious, that Ni has accumulated at this area, whereas some Al is missing. Apart from that, the Fe content is slightly elevated at the expense of Cr.

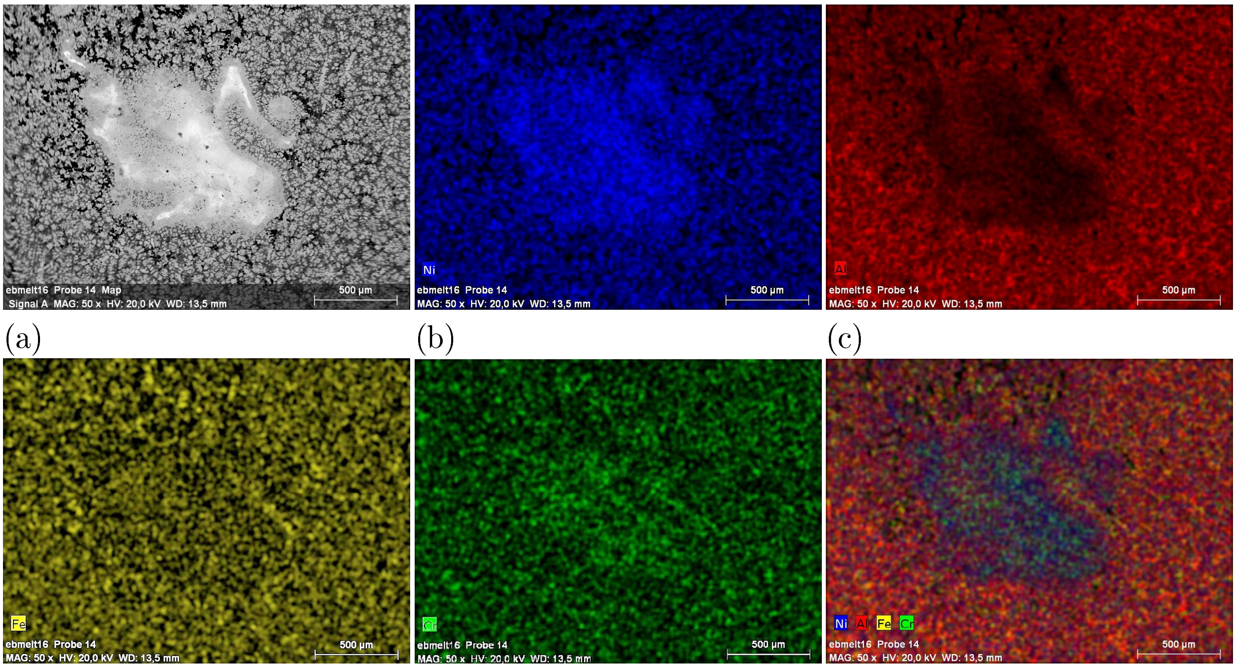

(a) (b) (c)

(c) (d) (f)

Figure 4.15: (a) BSE-image (b) Ni (c) Al (d) Fe (e) Cr (f) all 4 elements

Although the nugget is mainly homogeneous, some segregations are still visible. When performing further melting cycles, the nugget will remelt, distributing the elements uniformly.

Microhardness Measurement HV

In order to obtain more detailed information about the different phases, microhardness measurements were performed (Figure 4.16).

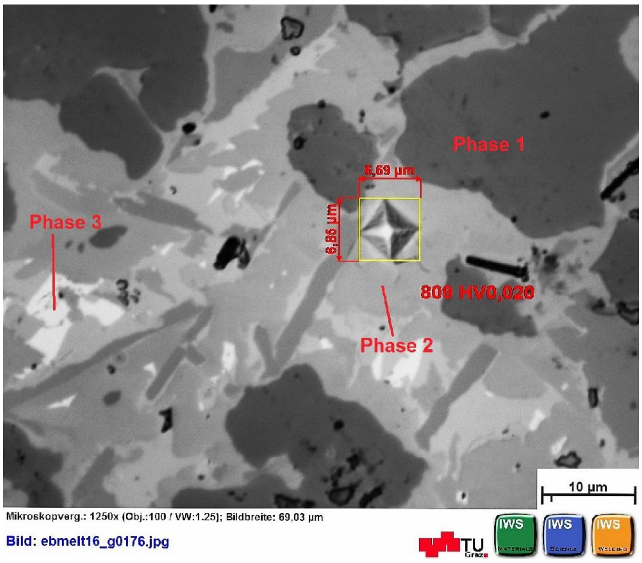

	HV0.020
Phase 1	1,029 ± 35
Phase 2	776 ± 43
Phase 3	n/a

Figure 4.16: Vickers microhardness measurements of the three phases marked in the left image.

Due to the small size, the microhardness of Phase 3 cannot be measured. When measuring Phase 2, cracks occurred during each hardness test. Thus, it can be assumed, that the values are slightly modified. Phase 2 is apparently very brittle and hard (HV = 776 ± 43). According to the measurements in Figure 4.16, Phase 1 shows the highest hardness (HV = 1,029 ± 35). Unfortunately, no values for this specific alloy is discussed in literature. Therefore, the measured values could not be compared.

Influence of the oxidised Base Material

Subsequent to an unsuccessful attempt to grind the Al granulate, the effect of surface oxides on the melting process could accidentally be observed. During milling the Al powder was exposed to air for too long. The following EBW parameters were chosen as usual to melt Ni (m_{Ni} = 2.02 g) and Al (m_{Al} = 2.01 g):

Table 4.10: EBW parameters for both melting cycles

U_A [kV]	**I_B [mA]**	**A [mm]**	**t_B [s]**	**f [Hz]**	**Figure**	**m_{start}[g]**	**m_{final} [g]**
120	3.00	19 x 19	30	1,000	Spirale10000	4.04	-

Even the first melting cycle showed an unusual behaviour compared to previous experiments (Figure 4.17). After 1 s a cluster with an uneven shape was observed (a). This structure improved a bit during the next seconds of processing. A substantial fraction of the starting material did not melt or even incandescence (b). It took more than 7 s until this fraction finally started to melt (c). Afterwards the bulky nugget began to solidify quite evenly during the remaining time (d)-(f). Obviously the shape was still not as expected and a noticeable amount of non-molten powder remained in the crucible.

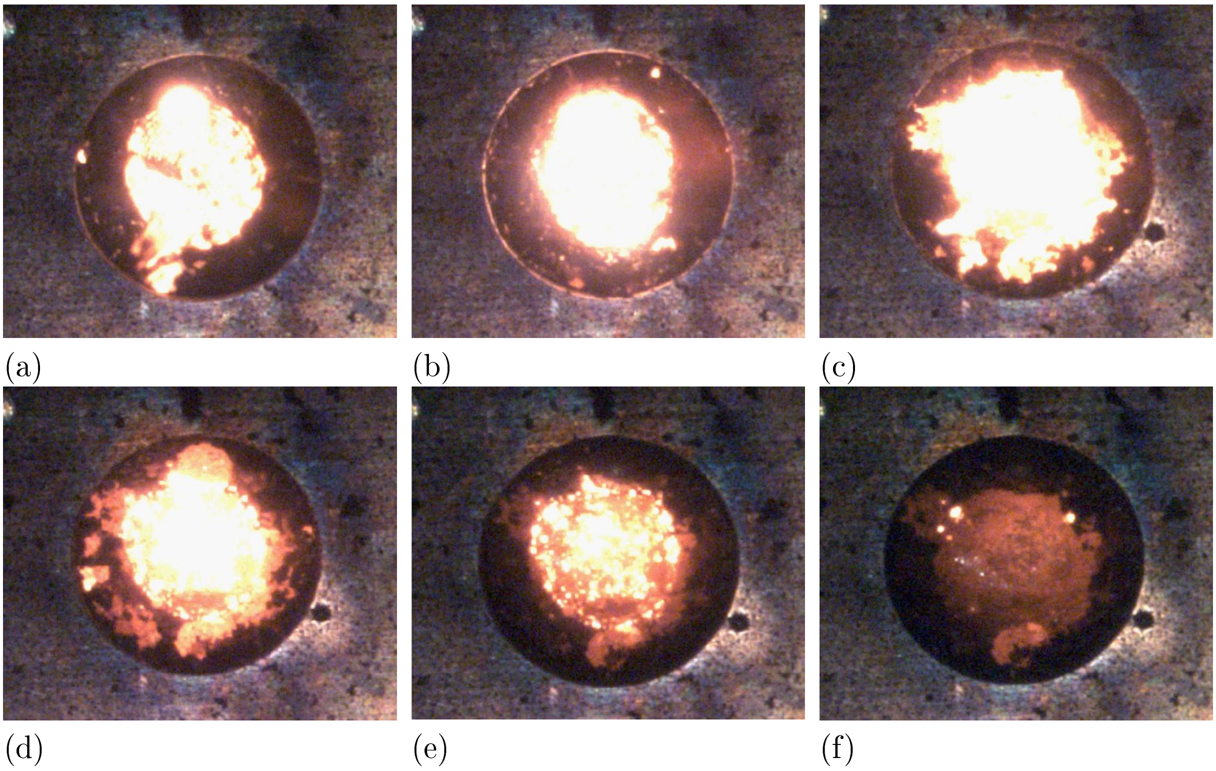
(a) (b) (c)
(d) (e) (f)

Figure 4.17: Different steps of the first melting cycle with oxidised aluminium (a) 1 s (b) 2 s (c) 7 s (d) 9 s (e) 11 s (f) 12 s.

Before starting with the second melting cycle the excessive granulate was removed. The same parameters were used again, only the time was elevated (t = 40 s). After around 4 s a minor part in the centre of the nugget melted up (a) followed by the fusion of the adjacent areas (b). Eventually, the whole sample glowed steady and defects on the surface melted as well (c). After 12 s the sample expanded and exploded ((d), (e)). The crucible was left completely empty, no material remained (f).

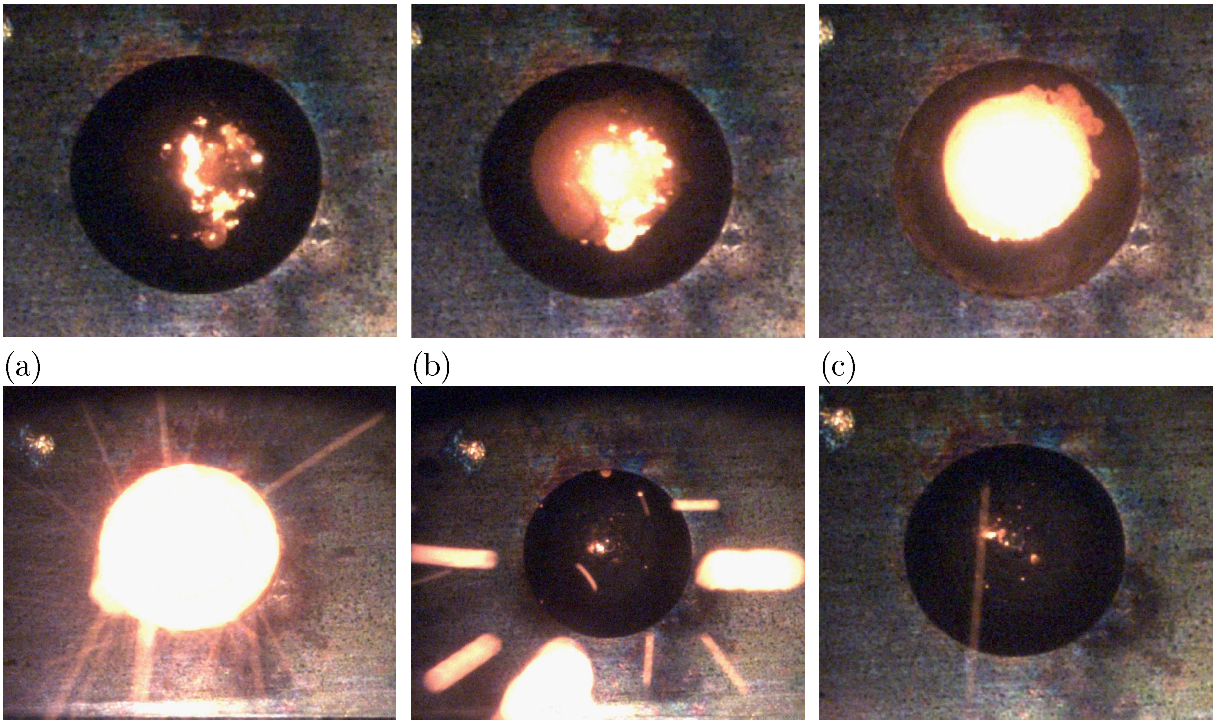
(a) (b) (c) (d) (e) (f)

Figure 4.18: Different steps of the second melting cycle with oxidised aluminium (a) 4 s (b) 6 s (c) 9 s (d) 12 s (e) 12 s (f) 14 s.

The results demonstrated the influence of the different melting points of pure Al (T_m = 660 °C) and Al_2O_3 (T_m = 2,072 °C). Since granulate was exposed to air for too long, a thick oxide layer was formed on the surface of the grains. When the electron beam is directed onto the powder, the pure Al starts to melt, whereas the Al_2O_3 layer remains solid and acts as an insulator. As a result of the continuing energy input by the electron beam Al starts to evaporate within the sphere, building up pressure. At the same time the oxide layer cracks due to its high brittleness, resulting in the explosive outburst.

4.3 Catalytic Test

4.3.1 Preparation for Catalytic Test

The processing steps, that were necessary to manufacture an electrode are listed in the following Figure 4.19.

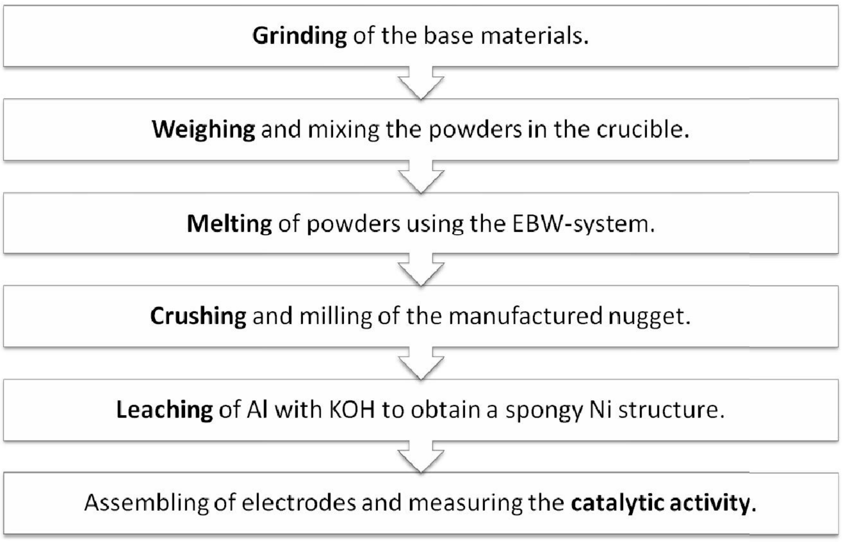

Figure 4.19: Abstract of the manufacturing steps

In order to investigate the catalytic activity of the manufactured alloy in fuel cells the nuggets had to be crushed and milled to a fine powder. Before milling the nugget in ball mill it was pulverised with a mechanical press. By further grinding of the alloy the particle size could be reduced to a size <25 μm.

Figure 4.20: (a) Press at the IWS and (b) nugget after pressing

After grinding, the Al was leached out of the alloy with a potassium hydroxide solution (KOH) to obtain a spongy structure. In this state the sample is highly pyrophoric and thus had to be deactivated by partial oxidation, i.e. passivation of the surface. After manufacturing of the fuel cell electrodes, the skeletal Ni was activated by a reducing current and simultaneous hydrogen supply.

In the following Figure 4.21 a BSE-image of the powder obtained after grinding the alloy nugget is shown (left). For comparison, an image of the powder after leaching is displayed as well (right). It has to be mentioned, that the leached powder is highly pyrophoric. Thus, it had to be passivated first.

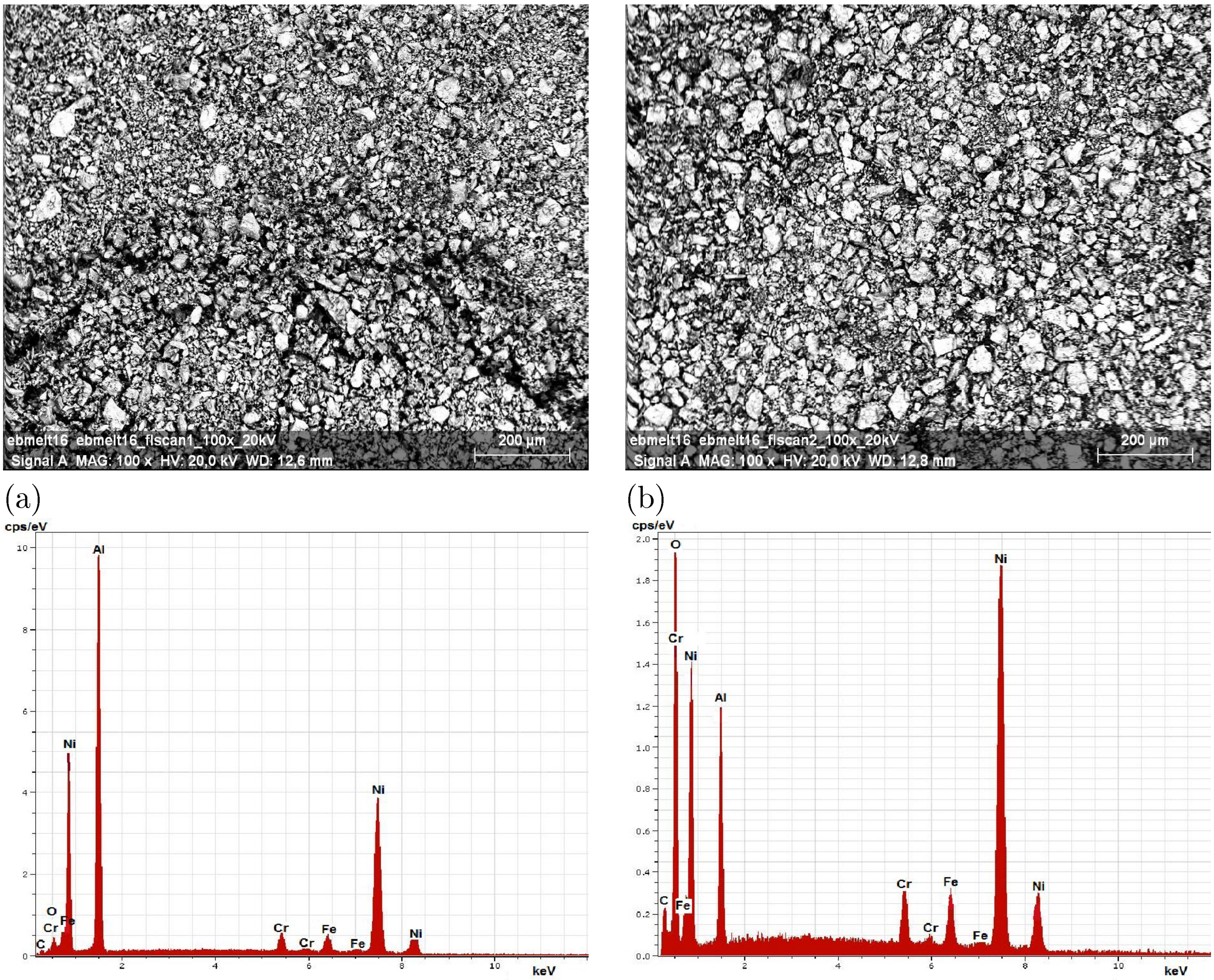

(a) (b)

(c) (d)

Figure 4.21: (a) BSE-image of the grinded Ni-Al-Fe-Cr powder before leaching (b) BSE-image of the leached and passivated Ni-Al-Fe-Cr powder (c) EDX-spectrum of the grinded Ni-Al-Fe-Cr powder before leaching (d) EDX-spectrum of the leached and passivated Ni-Al-Fe-Cr powder

Additionally, EDX-spectra of the selected areas have been recorded to obtain information about the elemental composition. It is substantial to keep in mind, that the scalings of the y-axis is different in the two plots. The compositions of the area scans are listed in the following Table 4.11.

Table 4.11: Composition of the powder before and after leaching.

	before leaching [%]	**after leaching [%]**
Ni	51	62
Al	41	11
Fe	4	5
Cr	3	4
O	-	16

It has to be mentioned, that the values have a high scattering. Accurate values can only be obtained, when the investigated surface is plain, dense, smooth and has a thickness bigger than the beam diameter. Since these requirements were not fulfilled, the obtained values can only give a hint about the composition and do not represent the exact values.

4.3.2 Measurement of Catalytic Activity

To measure the catalytic activity an electrode was assembled with the obtained spongy Ni powder. It was tested in a 3-electrode configuration recording the electrochemical characterisation. The Ni-electrode was serving as working electrode. The counter electrode consisted of stainless steel and a reversible hydrogen electrode was used as reference electrode. For comparison an electrode manufactured with a commercial Raney®-Ni catalyst was tested in the same set-up.

The current voltage characteristic of the skeletal Ni was recorded and is shown in Figure 4.22. The IV curve of the constructed anode shows a very high performance after 40 h of activation at 40 °C:

Current density	**Potential**	**Temperature**
86 $mA.cm^{-2}$	at 40 mV	40 °C
214 $mA.cm^{-2}$	at 120 mV	40 °C

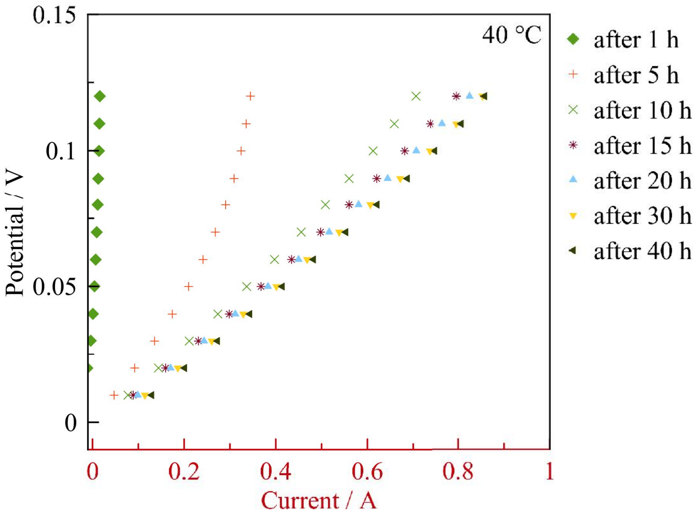

Figure 4.22: IV curve of the manufactured anode after 40 h of activation at 40 °C

Additionally, a long-term measurement was operated. The graph in Figure 4.23 shows again a high performance at 40 mV and 40 °C:

Time	**Current density**	**Potential**	**Temperature**
0 h	84 mA.cm^{-2}	at 40 mV	40 °C
40 h	93 mA.cm^{-2}	at 40 mV	40 °C

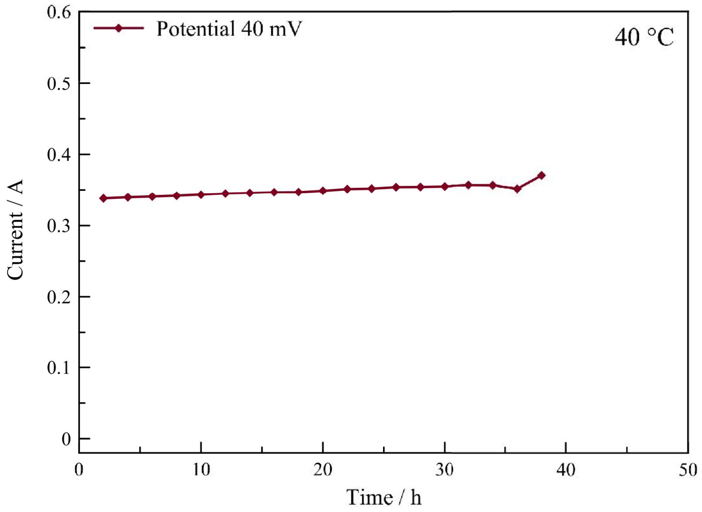

Figure 4.23: Long-term measurement at 40 mV and 40 °C

Comparison with Commercial Catalyst

Furthermore, the catalytic activity of an electrode manufactured of a commercial Raney®-Ni is plotted in Figure 4.24 below.

Current density	Potential	Temperature
96 $mA.cm^{-2}$	at 40 mV	40 °C
232 $mA.cm^{-2}$	at 120 mV	40 °C

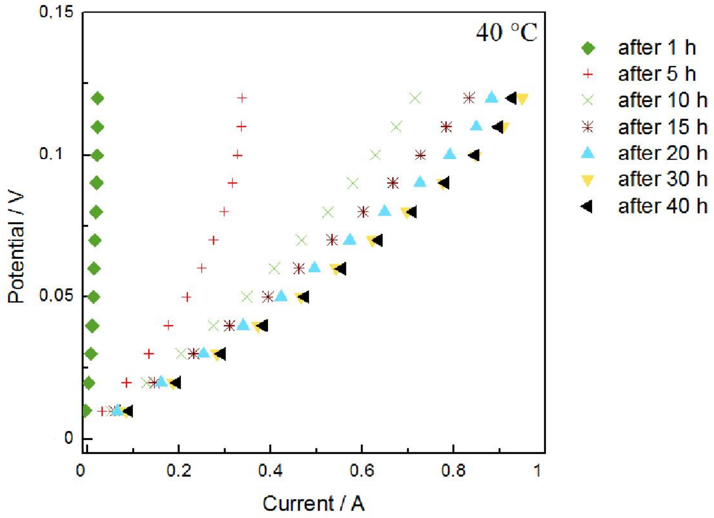

Figure 4.24: IV curve of the electrode manufactured with the Raney®-Ni catalyst (Sigma Aldrich) after 40 h of activation at 40 °C

The current voltage characteristic of the leached alloy manufactured with EBM (Figure 4.22 was compared with the IV curve of the commercial Raney®-Ni (Figure 4.24).

According to the plots, the performance of the spongy nickel manufactured with EBM is comparable to the performance of the electrodes manufactured with commercial Raney®-Ni catalyst.

5 Conclusion and Outlook

In this thesis Ni, Al, Fe and Cr were melted using EBM. The manufactured alloy nugget was then crushed and milled. The Al was leached with potassium hydroxide solution to obtain a spongy Ni-structure. With this alloy an electrode was manufactured to test the catalytic activity in a fuel cell.

Firstly, the melting parameters and preparation of the base material had to be optimised. New crucibles were manufactured to obtain bigger nuggets and facilitate the process. To investigate whether there is any drag-out of the fine granular powder or not, initial floating tests were performed. The mass losses did not exceed 8%, thus it was assumed to be negligible for the following tests.

In the course of the experiments it turned out, that melting with frequencies of 500 Hz, 1,000 Hz and 2,000 Hz deliver the best results. The mass loss is constant throughout the selected frequency range. Another experimental series was carried out to investigate the influence of different beam currents. With increasing beam current, the resulting alloy nugget is more uniform, but the mass loss of the powder increases.

Investigations of the manufactured Ni-Al nugget showed, that the major part of the microstructure after two melting cycles is homogeneous. However, some segregations are still observable. By applying further melting cycles, these segregations will dissolve. In addition, porosities were obtained throughout the sample. Since the nugget was grinded afterwards for further processing, this is negligible. EDX-analysis were performed to gather more information about the three phases appearing in the microstructure. Additionally, microhardness measurements of these phases showed, that two of the phases have a very high microhardness (Phase 1: 832 ± 46 HV, Phase 2: 1,023 ± 59 HV). However, Phase 3 is apparently so small, that no useful results could be obtained. Thus, an upper limit was estimated ($\leq$ 118 HV).

Subsequently, the manufactured Ni-Al-Fe-Cr nugget was investigated as well. Light microscopy-images showed a mainly homogeneous microstructure throughout the sample. Again, segregations are visible, as well as some pores. Furthermore, EDX-analysis of the three phases in the microstructure were performed. Elemental mapping showed an inhomogeneous distribution of the four elements within the selected segregation. Additionally, the microhardness of the three phases was similar to the phases observed Ni-Al alloy (Phase 1: 1,029 ± 35 HV, Phase 2: 776 ± 43 HV). The microhardness of Phase 3 could not be measured, due to its small area.

Grinding the coarse granulate of the starting materials is beneficial to facilitate the uniform distribution of all four elements in the crucibles. However, it has to be taken into account, that Al should not be exposed to air for too long. Due to the different melting points of pure Al and Al_2O_3, excessive oxidation of the Al granulate can cause an explosive outburst. Additionally, avoiding electrostatic charging is crucial.

With the ideal parameter identified during the previous experiments, nuggets were manufactured, crushed, milled and leached. The obtained spongy Ni is highly pyrophoric. Thus, it had to be passivated to enable the manufacturing of electrodes. The spongy Ni was then activated by a reducing current and simultaneous hydrogen supply to measure the catalytic activity. The current-voltage characteristic showed a very high performance after 40 h at 40 °C.

Due to the promising results, further investigations are recommended to obtain more detailed information about the properties of the fused alloy. Especially the determination of the phases appearing in the microstructures is of interest. In this context, it will be interesting to understand, the formation of the different phases. The thermodynamics can be further simulated using programs like MatCalc.

Further information on the alloys could be obtained by crushing the manufactured alloy using a tension-compression testing unit to record a stress-strain curve. Thereby, the stress, that is necessary to crush the nugget alloy can be determined.

To obtain improved results, different post-heat treatments can be applied on the nugget. The influence on the microstructure should then be investigated and a suitable post-heating identified. This heat treatment can either be done using the EBW right after the melting or separately in a chamber furnace with controlled temperature histogram. In addition, the influence of different cooling rates can be investigated as well.

As mentioned above, the preparation of the base materials influences the resulting nugget at a very high degree. Thus, further investigations are crucial for understanding and controlling the melting process. This is one important step to provide high reproducibility of the alloy manufacturing. Therefore, the investigation of external factors like temperature and humidity during the preparation step will be necessary. Additionally, further occurring effects need to be identified. The tools used for transporting the powder and processing might have an impact on the resulting alloy nugget as well.

After identification of the influencing factors mentioned above, further nuggets can be manufactured. The catalytic activity should then be recorded and compared to determine, whether there is an improvement in the activity or not.

6 List of Abbreviations

EBW	Electron Beam Welding
EBM	Electron Beam Melting
FC	Fuel Cell
AFC	Alkaline Fuel Cell
SEM	Scanning Electron Microscopy
SE	Secondary Electrons
BSE	Back Scattered Electrons
Z	Atomic Number
EDX	Energy dispersive X-ray Spectroscopy
HV	Vickers Hardness
fcc	Face-centered cubic
bcc	Body-centered cubic
MA	Mechanical Alloying
TZM	Titanium Zirconium Molybdenum
LOM	Light Optical Microscopy

List of Figures

List of Tables

Bibliography

[1] The World Bank. Electric power consumption (kWh per capita). *http://data.worldbank.org/indicator/EG.USE.ELEC.KH.PC*. Accessed: 2016-05-06.

[2] United States Environmental Protection Agency (EPA). U.S. Greenhouse Gas Inventory Report: 1990-2014. *https://www3.epa.gov/climatechange/ghgemissions/usinventoryreport.html*. Accessed: 2016-05-06.

[3] Volker Adam, Uwe Clauß, and et al. *Electron Beam Welding: The fundamentals of a fascinating technology*. pro-beam AG & Co. KGaA, 2011.

[4] Peter Petrov, Chavdar Georgiev, and Georgy Petrov. Experimental investigation of weld pool formation in electron beam welding. *Vacuum*, 51:339–343, 1998.

[5] H. Schultz. *Electron beam welding*. Abington Publishing, 1993.

[6] N. Ahmed. *New Developments in Advanced Welding*. Woodhead Publishing Limited, 2005.

[7] M. Kahnert. *Scanstrategien zur verbesserten Prozessführung beim Elektronenstrahlschmelzen (EBM)*. PhD thesis, Technische Universität München, 2014.

[8] James Larminie and Andrew Dicks. *Fuel Cell Systems Explained*. John Wiley & Sons Ltd, 2003.

[9] Sossina M. Haile. Fuel cell materials and components. *Acta Materialia*, 51:5981–6000, 2003.

[10] Y. Kiros and S. Schwartz. Long-term hydrogen oxidation catalysts in alkaline fuel cells. *Journal of Power Sources*, 87:101–105, 2000.

[11] Peter Kurzweil. *Brennstoffzellentechnik: Grundlagen, Komponenten, Systeme, Anwendungen*. Springer Vieweg, Wiesbaden, 2013.

[12] G.F. McLean, T. Niet, S. Prince-Richard, and N. Djilali. An assessment of alkaline fuel cell technology. *International Journal of Hydrogen Energy*, 27:507–526, 2002.

[13] Sabine Schweizer, Robin Chaudret, John Low, and Lalitha Subramanian. Molecular modeling and simulation of Raney Nickel: From alloy precursor to the final porous catalyst. *Computational Materials Science*, 99:336–342, 2014.

[14] H.J. Bargel and G. Schulze. *Werkstoffkunde*. VDI-Verlag GmbH, 1994.

[15] Group of Inorganic Chemistry and Catalysis. *http://www.inorganic-chemistry-and-catalysis.eu/people/technical-staff/marjan-versluijs-helder/home.html*. Accessed: 2016-05-09.

[16] The University of Iowa. Central Microscopy. *http://cmrf.research.uiowa.edu/scanning-electron-microscopy.* Accessed: 2016-04-10.

[17] L. Reimer. *Scanning Electron Microscopy: Physics of Image Formation and Microanalysis.* Springer-Verlag, 1998.

[18] Lawrence C. Wagner. *Failure Analysis of Integrated Circuits.* Springer US, 1999.

[19] Virginia Tech Sustainable Nanotechnology. Transmission Electron Microscopy: Application in environmental nanoscience. *http://blogs.lt.vt.edu/sustainablenano/2015/02/09/transmission-electron-microscopy-application-in-environmental-nanoscience/.* Accessed: 2016-04-11.

[20] Nasser Kanani and et al. *Moderne Mess- und Prüfverfahren für metallische und andere anorganische Überzüge.* expert verlag, 2007.

[21] Lenntech. Periodensystem der Elemente. *http://www.lenntech.de/pse/pse.htm.* Accessed: 2016-05-10.

[22] Formelsammlung und Berechnungsprogramme für Anlagenbau. *http://www.schweizer-fn.de/stoff/wleit_metall/wleit_metall.php*. Accessed: 2016-05-10.

[23] Schmelzwärme. *http://www.chemie.de/lexikon/.* Accessed: 2016-05-10.

[24] K.E. Volk. *Nickel und Nickellegierungen: Eigenschaften und Verhalten.* Springer-Verlag Berlin Heidelberg GmbH, 1970.

[25] Theodore Gray. Periodic table. *periodictable.com.* Accessed: 2016-05-10.

[26] G. Gottstein. *Physikalische Grundlagen der Materialkunde.* Springer-Verlag, 2007.

[27] Products from Sigma-Aldrich. *http://www.sigmaaldrich.com/catalog/.* Accessed: 2016-05-10.

[28] Chemgaroo-ChemgaPedia. *www.chemgapedia.de.* Accessed: 2016-06-16.

[29] Josh Kimmel. Evaluation of Composition and Phases in Platinum Aluminide Diffusion Coatings. *http://www.arrhenius.ucsd.edu/Josh/Josh_Kimmel.html.* Accessed: 2016-05-08.

[30] H.H. Ewe. Die Wasserstoffspeicherkapazität des Raney-Nickels. *Electrochimica Acta*, 17:2267–2275, 1972.

[31] V.N. Ermolaev, A.B. Fasman, and et al. Electron-Optical Investigation of the Formation of Skeletal Catalysts. *Bulletin of the Academy of Sciences of the USSR*, pages 1218–1222, 1983.

[32] Tahei Tomida and Ichira Nakabayashi. Spongy Raney Nickel Hydrogen Electrodes for Alkaline Fuel Cells. *J. Electrochem. Soc.*, 136(11):3296–3298, 1989.

[33] Beatriz Zeifert, Jose Salmones Blásquez, J. Gerardo Cabanas Moreno, and Hector A. Calderón. Raney-Nickel Catalysts Produced by Mechanical Alloying. *Rev. Adv. Mater. Sci.*, 18:632–638, 2008.

[34] Thomas Spenger. Diplomarbeit: Nutzung des Elektronenstrahlprozesses zur Herstellung von Modelllegierungen, 2015.

[35] bmwfw. Elektronenstrahlschweißen. *https://forschungsinfrastruktur.bmwfw.gv.at/de /institution/technische-universitat-graz_9?id=1480*. Accessed: 2016-05-10.

[36] Institut für Werkstoffkunde und Schweißtechnik. Die Elektronenstrahlschweißanlage EBW. *http://portal.tugraz.at/portal/page/portal/TU_Graz/Einrichtungen/Institute /Homepages/i3030/Labor/Schweisslabor/TechDatEBW*. Accessed: 2016-05-10.

[37] Products from Alfa Aesar. *https://www.alfa.com/de/catalog/*. Accessed: 2016-05-10.

[38] M. Konieczny, R. Mola, and et al. Processing, microstructure and properties of laminated Ni-intermetallic composites synthesised using Ni sheets and Al foils. *Archives of Metallurgy and Materials*, 56(3):693–702, 2011.